oxide synthase mediates the change from retinal to vitreal neovascularization in ischemic retinopathy. *J. Clin. Invest.*, **107**, 717-725 2001.

[37] Itoh, J., Kawai, K., Serizawa, A., Yasumura, K., Ogawa, K., and Osamura, R.Y.: A new approach to three-dimensional reconstructed imaging of hormone-secreting cells and their microvessel environments in rat pituitary glands by confocal laser scanning microscopy. *J. Histochem. Cytochem.*, **48**, 569-577, 2000.

[38] Itoh, J., Yasumasa, K., Takeshita, T., Ishikawa, H., Kobayashi, H., Ogawa, K., Kawai, K., Serizawa, A., and Osamura, R.Y.: Three-dimensional imaging of tumor angiogenesis. *Analyt. Quant. Cytol. Histol.*, **22**, 85-90, 2000.

[39] Kobzik, L., Reid, M.B., Bredt, D.S., and Stamler, J.S.: Nitric oxide in skeletal muscle. *Nature*, **372**, 546-548 1994.

[40] Brenman, J.E., Christopherson, K.S., Craven, S.E., McGee, A.W., and Bredt, D.S.: Cloning and Characterization of Postsynaptic Density 93, a Nitric Oxide Synthase Interacting Protein. *J. Neurosci.*, **16**, 7407-7415, 1996.

[41] Dreyer, J., Schleicher, M., Tappe, A., Schilling, K., Kuner, T., Kusumawidijaja, G., Müller-Esterl, W., Oess, S., and Kuner, R.: Nitric Oxide Synthase (NOS)-Interacting Protein Interacts with Neuronal NOS and Regulates Its Distribution and Activity. *J. Neurosci.*, **24**, 10454-10465, 2004.

[42] Sharshar, T., Gray, F., Geoffroy, L.G., Hopkinson, N.S., Ross, E., Dorandeu, A., Orlikowski, D., Raphael, J.C., Gajdos, P., and Annane, D.: Apoptosis of neurons in cardiovascular autonomic centres triggered by inducible nitric oxide synthase after death from septic shock. *Lancet*, **362**, 1799-1805 2003.

[43] Liang, F., Gao, E., Tao, L., Liu, H., Ou, Y., Christopher, T.A., Lopez, B.L., and Ma, X.L.: Critical timing of L-arginine treatment in post-ischemic myocardial apoptosis—role of NOS isoforms. *Cardiovasc. Res.*, **62**, 568-577, 2004.

[44] Kane, A.J., Barker, J.E., Mitchell, G.M., Theile, D.R.B., Romero, R., Messina, A., Wagh, M., Fraulin, F.O.G., Morrison, W.A., and Stewart, A.G.: Inducible nitric oxide synthase (iNOS) activity promotes ischemic skin flap survival. *Br. J. Pharmacol.*, **132**, 1631-1638, 2001.

[45] Cuzzocrea, S., Chatterjee, P.K., Mazzon, E., Dugo, L., De Sarro, A., Van de Loo, F.A., Caputi, A.P., and Thiemermann, C.: Role of induced nitric oxide in the initiation of the inflammatory response after postischemic injury. *Shock*, 18, 169-176, 2002.

[46] Bolli, R.: Cardioprotective function of inducible nitric oxide synthase and role of nitric oxide in myocardial ischemia and preconditioning: an overview of a decade of research. *J. Mol. Cell. Cardiol.*, 33, 1897-918, 2001.

[47] Kisley, L.R., Barrett, B.S., Bauer, A.K., Dwyer-Nield, L.D., Barthel, B., Meyer, A.M., Thompson, D.C., and Malkinson, A.M.: Genetic ablation of inducible nitric oxide synthase decreases mouse lung Tumorigenesis. *Cancer. Res.*, **62**, 6850-6856 2002.

[48] Deininger, M.H., Wybranietz, W.A., Graepler, F.T., Lauer, U.M., Meyermann, R., and Schluesener, H.J.: Endothelial endostatin release is induced by general cell stress and modulated by the nitric oxide/cGMP pathway. *F.A.S.E.B. J.*, **17**, 1267-1276 2003.

[49] Cianchi, F., Cortesini, C., Fantappiè, O., Messerini, L., Sardi, I., Lasagna, N., Perna, F., Fabbroni, V., Felice, A.D., Perigli, G., Mazzanti, R., and Masini, E.: Cyclooxygenase-2 activation mediates the proangiogenic effect of nitric oxide in colorectal cancer. *Clin. Cancer. Res.*, **10**, 2694-2704, 2004.

[50] Fukumura, D., Gohongi, T., Kadambi, A., Izumi, Y., Ang, J., Yun, C.O., Buerk, D.G., Huang, P.L., and Jain, R.K.: Predominant role of endothelial nitric oxide synthase in vascular endothelial growth factor-induced angiogenesis and vascular permeability. *Proc. Natl. Acad. Sci. U. S. A.*, **98**, 2604-2609, 2001.

[51] Qi, W., Chen, L.E., Zhang, L., Eu, J.P., Seaber, A.V., and Urbaniak, J.R.: Reperfusion injury in skeletal muscle is reduced in inducible nitric oxide synthase knockout mice. *J. Appl. Physiol.*, **97**, 1323-1328, 2004.

THYROID
Volume 16, Number 4, 2006

Triiodothyronine Acutely Increases Blood Flow in the Ventricles and Kidneys of Anesthesized Rabbits

Koji Kimura,[1] Yoshiro Shinozaki,[1] Sio Jujo,[1] Toru Shizuma,[2] Naoto Fukuyama,[1] and Hiroe Nakazawa[1]

Thyroid hormone (triiodothyronine [T_3]) has various nongenomic effects, including alterations in glucose and fatty acid metabolism, augmentation of intracellular Ca^{2+}, enhancement of myocardial contractility, and vascular dilatation. However, its effect on regional blood flow remains to be established. We have measured the effect of T_3 on blood flow in major organs of anesthetized rabbits *in vivo* using the microsphere method. Under artificial respiration, nonradioactive microspheres (5×10^5) labeled with barium were injected to measure blood flow at control level. Then, T_3 (50 μg/kg per milliliter) was administered and microspheres labeled with iodine (5×10^5) were injected. The atria, ventricles, kidneys, and right upper limb were excised and their contents of microspheres were evaluated. Blood flow in the ventricles was significantly increased by T_3 (2.9 ± 0.3 versus 3.4 ± 0.3 mL/min per gram, vehicle versus T_3). Similarly, blood flow in the kidneys was significantly higher after T_3 injection (4.3 ± 0.5 versus 5.1 ± 0.5 mL/min per, vehicle versus T_3). The blood flow in the atria and skeletal muscles remained unchanged. These results indicate that the vasodilatory response to T_3 is not uniform and occurs preferentially in major organs such as cardiac ventricles and kidneys; this may be relevant to the T_3-induced improvement of cardiac function.

Introduction

THYROID HORMONE (triiodothyronine [T_3]) exerts its effect by binding the specific receptor in the nucleus, and activating or repressing transcription of target genes. In addition to this genomic action, T_3 has nongenomic effects that occur very quickly upon T_3 exposure (1,2) and are insensitive to inhibitors of protein synthesis. Nongenomic effects include alterations in glucose (3) and fatty acid metabolism (4), increase in mitochondrial oxygen consumption (5), augmentation of intracellular Ca^{2+} (6–9), enhancement of myocardial contractility (10) and dilatation of vasculature (11–13). These effects have been demonstrated in cells or tissue *in vitro*, as well as in perfused heart preparations or *in vivo*. Of particular importance are the improvement of cardiac function in conscious dogs with pacing-induced cardiomyopathy (14) and the beneficial outcome in patients undergoing cardiopulmonary bypass (15). These results suggest that acute administration of T_3 may become a therapeutic option for patients with impaired ventricular function. A recent study (16) performed in volunteers provided further support for its use in the clinical situation, because T_3 administration acutely induced a decrease in systemic vascular resistance and an increase in cardiac output. This indicates that T_3 can produce acute arterial dilation in healthy euthyroid humans. However, further basic studies are required before clinical use, because important information remains to be obtained. One such point is whether or not the decrease in systemic vascular resistance actually increases regional blood flow. It is also important to examine whether the vasodilatory response to T_3 administration occurs uniformly in all organs.

The purpose of this study was to examine whether the vasodilatory effect of T_3 differs among various organs. To test this, we measured regional blood flow in major organs using the microsphere method *in vivo*.

Materials and Methods

Animals

Animals were managed in accordance with guiding principles for the care and use of animals proposed by the Physiological Society of Japan and the *American Journal of Physiology*.

Japanese White rabbits weighing 3.1 ± 0.1 kg were anesthetized with pentobarbital sodium (20 mg/kg intravenously), intubated, and ventilated with room air mixed with oxygen (0.5 L/min). Four catheters were placed: one in the left ventricle for microsphere injection, two in the femoral arteries for blood pressure measurement and blood sample

[1]Department of Physiology, School of Medicine, Tokai University, Isehara, Kanagawa, Japan.
[2]Institute of Gastroenterology, Tokyo Women's Medical University, Shinjuku-ku, Tokyo, Japan.

withdrawal, and one in the femoral vein for vehicle or T_3 injection. The blood pressure and electrocardiogram were continuously recorded throughout the experiment.

Experimental protocol

After stabilization of the hemodynamics, 1 mL of the vehicle of T_3 was administered (over 1 minute) and the first injection of 5×10^5 microspheres labeled with barium (Sekisui Plastic Co. Ltd., Japan) was made 5 minutes after the vehicle injection. Then T_3 (50 μg/kg per milliliter; 144.3–177 μg/mL) was administered over 1 minute and the second injection of 5×10^5 microspheres labeled with iodine was made 5 minutes after T_3 injection. In an additional four rabbits microspheres were injected 5 minutes and 30 minutes after T_3 injection to observe time course of T_3 effect. At the end of the experiment, the rabbits were sacrificed with an overdose of pentobarbital sodium, and the heart, kidneys, and skeletal muscles of the right upper limb were removed for blood flow measurements.

Measurements of regional blood flow

Regional blood flow was determined by the nonradioactive microsphere technique, as previously reported (17). Briefly, heavy metal microspheres (barium and iodine 15 μm optical density [OD], 5×10^5) suspended in 1 mL of normal saline containing 0.05% Tween 80 were infused into the left ventricle for 1 minute, followed by flushing with 0.5 mL of saline for 30 seconds. Withdrawal of reference blood from the femoral artery was continued for 30 seconds after the saline flush was completed. Each of the tissues and the reference blood samples was dissolved completely in 2 N KOH solution in a vial. The vials were centrifuged and the microspheres were aspirated and transferred to the surface of filter paper under vacuum. Heavy metals on the paper were quantitated by x-ray fluorescence spectrometry (PW1480, Phillips, Almelo, The Netherlands) (17). We used microspheres labeled with barium (Ba) in the first injection and iodine (I) in the second injection. In preliminary experiments we confirmed that this number of microspheres (5×10^5) did not impair the microcirculation, and provided sufficient sensitivity of evaluation in this size of rabbit.

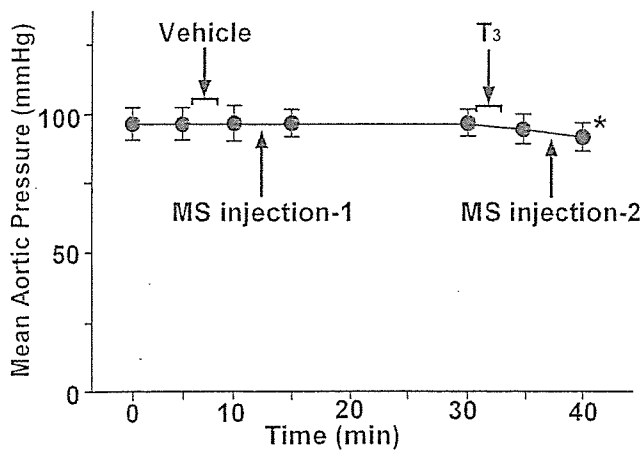

FIG. 1. Time course of blood pressure in four rabbits. Arrows indicate timing of each injection. MS injection 1, barium microspheres injection (5×10^5); MS injection 2, iodine microspheres injection (5×10^5); vehicle, vehicle of triiodothyronine (T_3) solution injection (1 mL); T_3, T_3 injection (50 μg/kg, 1 mL). *Indicates significant difference between blood pressure prior to T_3 injection and that 10 minutes after T_3 injection.

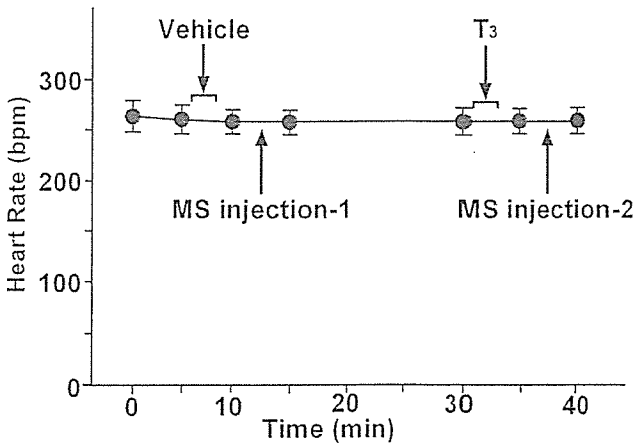

FIG. 2. Time course of heart rate. MS injection 1, barium microspheres injection (5×10^5); MS injection 2, iodine microspheres injection (5×10^5); vehicle, vehicle of triiodothyronine (T_3) solution injection (1 mL); T_3, T_3 injection (50 μg/kg, 1 mL). *Indicates significant difference between blood pressure prior to T_3 injection and that 10 minutes after T_3 injection.

The stock solution of T_3 (Sigma, St. Louis, MO) was prepared fresh each day and serially diluted to the necessary concentrations. The free T_3 level in plasma was measured with a commercial electrochemiluminescence assay (ECLIA; Roche Molecular Biochemicals, Mannheim, Germany).

Statistics

All results are presented as means ± standard error (SE). A paired t test was used to compare the data before and after T_3 injection. A p value of less than 0.05 was considered significant.

Results

The basal plasma free T_3 level was 3.23 ± 0.28 (range, 2.4–3.63) pg/mL, and free T_3 increased to over 32.6 pg/mL at 20 minutes after T_3 injection. As T_3 exceeded the upper quantitation limit of the test (32.6 μg/mL), peak values could not be determined

Figure 1 shows the time course of mean blood pressure during the experiment. Vehicle injection did not affect the blood pressure (96.5 ± 5.9 and 97.0 ± 5.9 mm Hg before and after, respectively). Blood pressure prior to T_3 injection was 97.0 ± 4.3 mm Hg, and was slightly decreased at 5 minutes after the injection (94.5 ± 5.4 mm Hg). Blood pressure at 10 minutes after the injection was 91.2 ± 5.5 mm Hg (signifi-

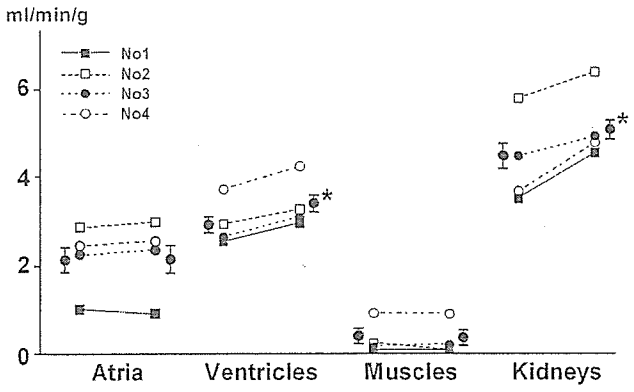

FIG. 3. Regional blood flow during vehicle and triiodothyronine (T_3) injections. Different symbols are used to indicate individual rabbits. *Indicates significant difference between vehicle and T_3 injections. ($p < 0.05$)

cantly lower than that prior to T_3 injection). Heart rate remained unaltered (Fig. 2). Figure 3 shows the changes in regional blood flow in four organs. T_3 injection increased blood flow to the ventricles and kidneys (ventricles: 2.9 ± 0.3 versus 3.4 ± 0.3 and kidneys: 4.3 ± 0.5 versus 5.1 ± 0.5 mL/min/g, before versus after T_3 injection), but the flows in the atria and skeletal muscles remained unchanged (atria: 2.1 ± 0.4 versus 2.2 ± 0.4 and muscles: 0.3 ± 0.2 versus 0.3 ± 0.3 mL/min/g, before versus after). In additional experiments to evaluate the time course of T_3 effect, barium was injected 5 minutes and iodine was injected 30 minutes after T_3 injection. Blood flows remained unchanged: 2.1 ± 0.2 versus 2.1 ± 0.3 in atria, 3.0 ± 0.3 versus 3.3 ± 0.2 in ventricle, 0.1 ± 0.2 versus 0.2 ± 0.2 in muscles, and 5.0 ± 0.3 versus 5.1 ± 0.4 in kidneys, indicating that the effect of T_3 lasted at least for 30 minutes.

Discussion

This is the first study to evaluate regional blood flows immediately after T_3 administration, and the results show that vasodilatory response to T_3 is diverse in various organs. Blood flow in the ventricles and kidneys increased, but that in atria and skeletal muscles remained unaffected. As the cardiovascular system is one of the major targets of genomic as well as nongenomic T_3 action (1,2), and the ventricles and kidneys are important for the cardiovascular system, the significant increase of blood flow in these organs appears to provide a basis for the T_3-induced improvement of cardiac function. No increase in blood flow to skeletal muscles appears to contradict to previous studies in which relaxation was observed in isolated skeletal muscle artery (13) and in cultured smooth muscle cells (11). However, experimental conditions differ markedly since both studies were performed in *in vitro*. Particularly dilatation of the artery by T_3 was evaluated under the preconstricted condition by thromboxane, in which vasodilatory effect appears to be easily demonstrable.

The mechanism of the increase in blood flow by T_3 is dilatation of relevant arteries because systemic blood pressure decreased. In addition, an increase in cardiac output through the positive inotropic effect of T_3 may have contributed, because a rapid increase in cardiac output or in contractility following T_3 administration has been demonstrated *in vitro* (6,7,10,18), *ex vivo* (4,19), and *in vivo* (20,21).

Studies that have shown acute beneficial effects of T_3 were performed in patients with impaired cardiac function or undergoing cardiopulmonary bypass (15,22), both of which conditions are known to decrease T_3 levels (the low T_3 syndrome). Several animal studies have found that T_3 administration did not cause any hemodynamic changes under basal conditions or in a normal thyroid state, but significant effects were seen in hearts subjected to ischemic injury or ischemia-reperfusion injury, or in a hypothyroid condition (14,20). Thus a noteworthy feature of this study is that the effect was observed in the euthyroid state.

A membrane-associated receptor of T_3 is necessary for T_3 to exert its acute effect, and its existence seems very likely, by analogy with the recent discovery of membrane receptors for progestins and estrogens, which has clarified the mechanism underlying the nongenomic actions of steroid hormone (23,24). In the presence of such membrane-associated T_3 receptors, acute effects should be manifested even under physiologic and euthyroid conditions. The recent novel discovery by Scanlan et al. (25) provided evidence that metabolite of T_3 act through G-protein–coupled receptor.

Heart rate remained unaltered by T_3 administration. This may appear peculiar, because tachycardia is one of the most common manifestations in hyperthyroidism. However, it is in agreement with a previous study in which heart rate was not changed by T_3 in an isolated perfused heart (19), even though a marked increase in left ventricular developed pressure was observed. A review (11) also commented on unchanged heart rate despite a significant decrease in peripheral vascular resistance after T_3 administration.

In conclusion, T_3-induced acute vasodilatation is accompanied by an increase in blood flow in the ventricles and kidneys, and this may be one of the mechanisms underlying the T_3-induced improvement of cardiac function.

Acknowledgments

The authors thank Ms. Y Shinozaki for expert technical assistance. This work was supported by Mitsui Life Social Welfare Foundation

References

1. Davis PJ, Davis FB 2002 Nongenomic actions of thyroid hormone on the heart. Thyroid 12:459–466.
2. Bassett JH, Harvey BC, Williams GR 2003 Mechanisms of thyroid hormone receptor-specific nuclear and extra nuclear actions. Mol Cell Endocrin 213:1-11.
3. Segal J 1989 A rapid, extranuclear effect of 3,5,3′-triiodothyronine on sugar uptake by several tissues in the rat in vivo. Evidence for a physiological role for the thyroid hormone action at the level of the plasma membrane. Endocrinology 124:2755–2764.
4. Liu Q, Clanachan AS, Lopaschuk GD 1998 Acute effects of triiodothyronine on glucose and fatty acid metabolism during reperfusion of ischemic rat hearts. Am J Physiol 275:E392–399.
5. Wrutniak-Cabello C, Casas F, Cabello G 2001 Thyroid hormone action in mitochondria. J Mol Endocrinol 26:67–77.
6. Segal J 1990 Calcium is the first messenger for the action of thyroid hormone at the level of the plasma membrane: first

evidence for an acute effect of thyroid hormone on calcium uptake in the heart. Endocrinology 126:2693–2702.
7. Davis PJ, Davis FB 1993 Acute cellular actions of thyroid hormone and myocardial function. Ann Thorac Surg 56:S16–23.
8. Gotzsche LB 1994 L-triiodothyronine acutely increases Ca^{2+} uptake in the isolated, perfused rat heart. Changes in L-type Ca^{2+} channels and beta-receptors during short- and long-term hyper- and hypothyroidism. Eur J Endocrinol 130: 171–179.
9. Segal J, Masalha S, Schwalb H, Merin G, Borman JB, Uretzky G 1996 Acute effect of thyroid hormone in the rat heart: Role of calcium. J Endocrinol 149:73–80.
10. Wang YG, Dedkova EN, Fiening JP, Ojamaa K, Blatter LA, Lipsius SL 2003 Acute exposure to thyroid hormone increases Na^+ current and intracellular Ca^{2+} in cat atrial myocytes. J Physiol 546:491–499.
11. Ojamaa K, Balkman C, Klein IL 1993 Acute effects of triiodothyronine on arterial smooth muscle cells. Ann Thorac Surg 56:S61–66.
12. Yoneda K, Takasu N, Higa S, Oshiro C, Oshiro Y, Shimabukuro M, et al. 1998 Direct effects of thyroid hormones on rat coronary artery: Nongenomic effects of triiodothyronine and thyroxine. Thyroid 8:609–613.
13. Park KW, Dai HB, Ojamaa K, Lowenstein E, Klein I, Sellke FW 1997 The direct vasomotor effect of thyroid hormones on rat skeletal muscle resistance arteries. Anesth Analg 85:734–738.
14. Jamall IN, Pagel PS, Hettrick DA, Lowe D, Kersten JR, Tessmer JP, et al. 1997 Positive inotropic and lusitropic effects of triiodothyronine in conscious dogs with pacing-induced cardiomyopathy. Anesthesiology 87:102–109.
15. Vavouranakis I, Sanoudos G, Manios A, Kalogeropoulou K, Sitaras K, Kokkinos C 1994 Triiodothyronine administration in coronary artery bypass surgery: Effect on hemodynamics. J Cardiovasc Surg 35:383–389.
16. Schmidt BM, Martin N, Georgens AC, Tillmann HC, Feuring M, Christ M, Wehling M 2002 Nongenomic cardiovascular effects of triiodothyronine in euthyroid male volunteers. J Clin Endocrinol Metab 87:1681–1686.
17. Mri H, Haruyama S, Shinozaki Y, Okino H, Iida A, Takanashi R, et al. 1992 New nonradioactive microspheres and more sensitive X-ray fluorescence to measure regional blood flow. Am J Physiol 263:H1946–9.
18. Dudley SC Jr, Baumgarten CM 1993 Bursting of cardiac sodium channels after acute exposure to 3,5,3′-triiodo-L-thyronine. Circ Res 73:301–313.
19. Tielens ET, Forder JR, Chatham JC, Marrelli SP, Ladenson PW 1996 Acute L-triiodothyronine administration potentiates inotropic responses to beta-adrenergic stimulation in the isolated perfused rat heart. Cardiovasc Res 32:306–310.
20. Dyke CM, Yeh T Jr, Lehman JD, Abd-Elfattah A, Ding M, Wechsler AS, Salter DR 1991 Triiodothyronine-enhanced left ventricular function after ischemic injury. Ann Thorac Surg 52:14–19.
21. Gotzsche LB 1994 Acute increase in cardiac performance after triiodothyronine: Blunted response in amiodarone-treated pigs. J Cardiovasc Pharmacol 23:141–148.
22. Novitzky D, Cooper DK, Barton CI, Greer A, Chaffin J, Grim J, Zuhdi N 1989 Triiodothyronine as an inotropic agent after open heart surgery. J Thorac Cardiovasc Surg 98:972–977.
23. Li L, Haynes MP, Bender JR 2003 Plasma membrane localization and function of the estrogen receptor alpha variant (ER46) in human endothelial cells. Proc Natl Acad Sci USA 100:4807–4812.
24. Zhu Y, Bond J, Thomas P 2003 Identification, classification, and partial characterization of genes in humans and other vertebrates homologous to a fish membrane progestin receptor. Proc Natl Acad Sci USA 100:2237–2242.
25. Scanlan TS, Suchland KL, Hart ME, Chiellini G, Huang Y, Kruzich PJ, Frascarelli S, Crossley DA, Bunzow JR, Ronca-Testoni S, Lin ET, Hatton D, Zucchi R, Grandy DK 2004 3-Iodothyronamine is an endogenous and rapid-acting derivative of thyroid hormone. Nat Med 10:638–642

Address reprint requests to:
Hiroe Nakazawa, M.D., Ph.D.
Department of Physiology
School of Medicine
Tokai University
Bohseidai
Isehara, 259-1193
Japan

E-mail: nakazawa@is.icc.u-tokai.ac.jp

KIMURA

AU1
Provide city in Japan for Sekisui Plastics.

Available online at www.sciencedirect.com
ScienceDirect
ELSEVIER
Neurochemistry International 49 (2006) 448–453
NEUROCHEMISTRY International
www.elsevier.com/locate/neuint

Effect of sustained limb ischemia on norepinephrine release from skeletal muscle sympathetic nerve endings

Yosuke Kuroko [a], Noriyuki Tokunaga [b], Toji Yamazaki [b,*], Tsuyoshi Akiyama [b], Kozo Ishino [a], Shunji Sano [a], Hidezo Mori [b]

[a] *Department of Cardiovascular Surgery, Okayama University Graduate School of Medicine and Dentistry, Okayama 700-8558, Japan*
[b] *Department of Cardiac Physiology, National Cardiovascular Center Research Institute, 5-7-1 Fujishiro-dai, Suita, Osaka 565-8565, Japan*

Received 8 October 2005; accepted 2 March 2006
Available online 24 April 2006

Abstract

Acute ischemia has been reported to impair sympathetic outflow distal to the ischemic area in various organs, whereas relatively little is known about this phenomenon in skeletal muscle. We examined how acute ischemia affects norepinephrine (NE) release at skeletal muscle sympathetic nerve endings. We implanted a dialysis probe into the adductor muscle in anesthetized rabbits and measured dialysate NE levels as an index of skeletal muscle interstitial NE levels. Regional ischemia was introduced by microsphere injection and ligation of the common iliac artery. The time courses of dialysate NE levels were examined during prolonged ischemia. Ischemia induced a decrease in the dialysate NE level (from 19 ± 4 to 2.0 ± 0 pg/ml, mean ± S.E.), and then a progressive increase in the dialysate NE level. The increment in the dialysate NE level was examined with local administration of desipramine (DMI, a membrane NE transport inhibitor), ω-conotoxin GVIA (CTX, an N-type Ca^{2+} channel blocker), or TMB-8 (an intracellular Ca^{2+} antagonist). At 4 h ischemia, the increment in the dialysate NE level (vehicle group, 143 ± 30 pg/ml) was suppressed by TMB-8 (25 ± 5 pg/ml) but not by DMI (128 ± 10 pg/ml) or CTX (122 ± 18 pg/ml). At 6 h ischemia, the increment in the dialysate NE level was not suppressed by the pretreatment. Ischemia induced biphasic responses in the skeletal muscle. Initial reduction of NE release may be mediated by an impairment of axonal conduction and/or NE release function, while in the later phase, the skeletal muscle ischemia-induced NE release was partly attributable to exocytosis via intracellular Ca^{2+} overload rather than opening of calcium channels or carrier mediated outward transport of NE.

Keywords: Catecholamine; Interstitial space; Microdialysis; Rabbit; Striate muscle

1. Introduction

Acute ischemia has been reported to be associated with impairment of the sympathetic tract (Schömig et al., 1984; Toyohara et al., 1986; Fujii et al., 2003). A well-known example is myocardial ischemia associated with impairment of the regional cardiac sympathetic nerve endings (Schömig et al., 1984; Ciuffo et al., 1985). Outward norepinephrine (NE) transport through uptake$_1$ carrier has been proposed as one of the main mechanisms responsible for ischemia-induced NE efflux from sympathetic nerve endings (Schömig et al., 1984; Akiyama and Yamazaki, 2001). However, little is known about the sympathetic impairment evoked by skeletal muscle ischemia. Histochemical and electrophysiological studies (Barker and Saito, 1981; Hill et al., 1996) have identified sympathetic innervation in skeletal muscle, which exerted actions on the regulation of regional blood flow and glucose metabolism (Thompson and Mohrman, 1983; Fagius and Berne, 1994). During and after exercise, muscle sympathetic nerve activity has been reported to be modulated by ischemia-induced metaboreceptor stimulation (Cornett et al., 2000; Cui et al., 2001). Furthermore, skeletal muscle may be exposed to prolonged severe ischemia (Welsh and Lindinger, 1993). Severe skeletal muscle ischemia occurs with trauma, vascular diseases, and compartment syndrome. It is so far unknown whether severe muscle ischemia induces excessive NE release from muscle sympathetic nerve endings.

In view of energy metabolism, cardiac ischemia is characterized by rapid deterioration of cardiac function, which has been linked to a fall in intracellular pH, increased levels of inorganic phosphate and reduction in free energy changes of ATP-hydrolysis (Mair, 1999). In contrast to cardiac muscle,

* Corresponding author. Tel.: +81 6 6833 5012; fax: +81 6 6872 8092.
E-mail address: yamazaki@ri.ncvc.go.jp (T. Yamazaki).

0197-0186/$ – see front matter © 2006 Elsevier Ltd. All rights reserved.
doi:10.1016/j.neuint.2006.03.004

energy requirements in skeletal muscle are dependent on exercise and are reduced in the resting state since only resting tone is maintained (Idström et al., 1990; Lindsay et al., 1990). Typically, prolonged skeletal muscle ischemia imposes a metabolic stress that results in a depletion of glycogen, high-energy phosphagen, and adenine nucleotides (Welsh and Lindinger, 1993). Thus, a differential time course of energy metabolism occurs in the skeletal muscle and cardiac myocardium. No studies have systematically characterized the impairment of sympathetic nerves in the skeletal muscle ischemia.

Recently, we reported that microdialysis technique with high-performance liquid chromatography is a sensitive and versatile method for monitoring interstitial NE concentrations in myocardial ischemic regions (Akiyama et al., 1991, 1993). Moreover, we applied microdialysis technique to skeletal muscle and have reported that skeletal muscle dialysate NE serves as an index of muscle sympathetic nerve activity (Tokunaga et al., 2003a). Using this method, we investigated how acute skeletal muscle ischemia affects NE release from skeletal muscle sympathetic nerve endings and the mechanism of skeletal muscle ischemia-induced NE release with regional pharmacological intervention.

2. Methods

2.1. Animal model

The investigation conformed with the *Guide for the Care and Use of Laboratory Animals* published by the US National Institutes of Health (NIH Publication No. 85-23, revised 1996). Forty-two male Japanese white rabbits weighing 2.2–3.8 kg were used for the model of skeletal muscle ischemia. The animals were anesthetized with pentobarbital sodium (30–35 mg/kg) and ventilated with room air mixed with oxygen. The level of anesthesia was maintained with a continuous intravenous infusion of pentobarbital sodium (1–2 mg/kg/h). Body temperature was maintained with a heated pad and lamp. An electrocardiogram, heart rate (HR), and mean arterial blood pressure (MAP) were simultaneously monitored with a data recorder. After a longitudinal skin incision was made in the left groin, the dialysis probes were implanted in the left adductor muscle with a fine guiding needle.

2.2. Dialysis technique and NE measurements

With the dialysis technique, dialysate NE levels were measured as an index of skeletal muscle interstitial NE levels. For skeletal muscle dialysis, we designed a transverse dialysis probe. The dialysis fiber (13 mm length, 0.31 mm o.d. and 0.2 mm i.d.; PAN-1200, 50,000 molecular mass cut-off, Asahi Chemical, Tokyo, Japan) was glued at both ends into a polyethylene tube (25 cm length, 0.5 mm o.d. and 0.2 mm i.d.) (Akiyama et al., 1991). The dialysis probe was perfused with Ringer solution using a microinjection pump (CMA 102, Carnegie Medicin, Stockholm, Sweden). Similar to previous studies (Tokunaga et al., 2003a, 2003b), we chose a perfusion speed of 10 μl/min for skeletal muscle. Sampling periods were set at 15 min for skeletal muscle. Dialysate NE levels were measured by high-performance liquid chromatography with electrochemical detection (ECD-300, Eicom, Kyoto, Japan) after removing interfering compounds in the dialysate by an alumina procedure (Anton and Sayer, 1962; Akiyama et al., 1991). Dialysate dihydroxyphenylglycol (DHPG) levels were measured by separate high-performance liquid chromatography with electrochemical detection (Akiyama and Yamazaki, 2001).

2.3. Experimental protocols

Acute skeletal muscle ischemia was induced by injection of non-radioactive iodine-labeled microspheres (15 μm in diameter, 3×10^7/kg, Sekisui Plastic, Osaka, Japan) through the left common iliac artery, as previously described (Tanaka et al., 2000). After the injection of microspheres, the common iliac artery was ligated.

2.3.1. Protocol 1: time courses of dialysate NE levels during acute ischemia

To examine the time courses of dialysate NE levels during acute skeletal muscle ischemia, we measured dialysate NE levels over 60-min periods of skeletal muscle ischemia ($n = 6$). We collected four consecutive 15-min dialysate samples. Furthermore, we measured dialysate NE samples over a period of 6 h of skeletal muscle ischemia with 2 h interval in separate rabbits. To examine intraneuronal NE kinetics in the skeletal muscle, the measurement of dialysate DHPG level was added during 6 h of skeletal muscle ischemia ($n = 6$).

2.3.2. Protocol 2: involvement of NE uptake$_1$ transport, Ca^{2+} channels and cytosol Ca^{2+} in dialysate NE levels during acute ischemia

To examine the mechanism underlying the increment of NE release during the prolonged ischemia, dialysate NE levels were measured with regional pharmacological intervention. Neurotransmitter release from sympathetic nerve endings can be caused by a variety of different mechanisms (Schömig et al., 1987; Kawada et al., 2000; Akiyama and Yamazaki, 2001). In the present studies, we examined the roles of membrane NE transport, N-type Ca^{2+} channels and cytosol Ca^{2+} in the time courses of dialysate NE levels during prolonged ischemia. To examine the involvement of membrane NE transport in the ischemia-induced NE release, we locally administered an uptake$_1$ carrier blocker, desipramine (100 μM) through a dialysis probe and observed the responses of dialysate NE (Akiyama and Yamazaki, 2001) ($n = 6$). The same protocol was performed with addition of a voltage-dependent N-type Ca^{2+} channel blocker, ω-conotoxin GVIA (10 μM) ($n = 6$) or intracellular Ca^{2+} antagonist, 8-(*N*,*N*-diethylamino)-octyl-3,4,5-trimethoxybenzoate hydrochloride (TMB-8, 1 mM) ($n = 6$) through a dialysis probe. From data on protocol 1, we observed increases in dialysate NE levels after 2 h of skeletal muscle ischemia. Therefore, the time course of dialysate NE for skeletal muscle ischemia was examined over a period of 6 h with a 2 h-interval ($n = 6$). The effectiveness of ω-conotoxin GVIA (10 μM) ($n = 6$) or TMB-8 (1 mM) ($n = 6$) was tested before the experiment in separate rabbits. We administered high potassium (KCl, 100 mM) locally through the dialysis probe, and the dialysate NE response was obtained in the presence and absence of ω-conotoxin GVIA or TMB-8. High-K increased dialysate NE from 11.7 ± 2.8 to 84.7 ± 20.8 pg/ml ($n = 6$). This KCl-induced increment in dialysate NE was attenuated by the addition of ω-conotoxin GVIA or TMB-8 (Fig. 1).

2.3.3. Protocol 3: time courses of dialysate lactate levels during the hind limb ischemia

To confirm whether this perturbation induces tissue ischemia, we examined the time course of dialysate lactate levels as an index of tissue ischemia. The dialysate lactate levels were measured by kinetic enzymatic analysis with CMA 600 (Carnegie Medicin). In the skeletal muscle ischemia, four consecutive 15-

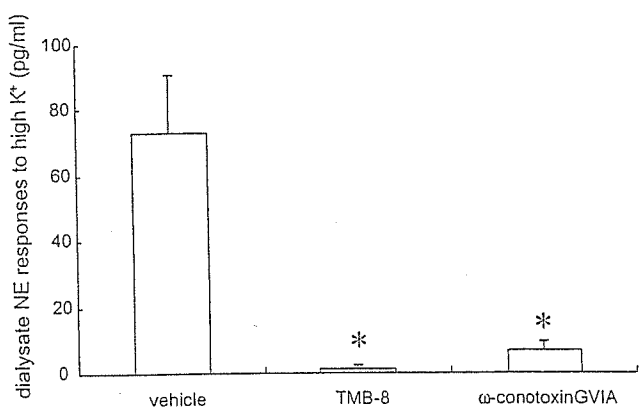

Fig. 1. Effects of pharmacological intervention on dialysate norepinephrine (NE) responses to high K^+ (KCl, 100 mM). Both TMB-8 (1 mM) and ω-conotoxin (10 μM) suppressed dialysate responses to high K^+. Values are means ± S.E. ($n = 6$).

min dialysate samples were collected during the initial 60-min and subsequently three consecutive samples were collected over a period of 6 h with a 2 h-interval ($n = 6$).

2.4. Statistical analysis

All data are presented as mean ± S.E. values. Hemodynamic and dialysate data responses to acute ischemia were statistically analyzed by analysis of variance with repeated measures. When a statistically significant effect of ischemia was detected as a whole, the Dunnett's test was applied to determine which mean values differed significantly from the control level. When a statistically significant effect of the treatment was detected, Newman–Keuls test was applied to determine which treatment differed significantly from the vehicle.

3. Results

Table 1 summarizes changes in HR and MAP. MAP and HR increased during 6 h-hind limb ischemia. Changes in MAP at 2 h and HR at 6 h-hind limb ischemia were significant.

3.1. Time courses of dialysate NE levels during short and prolonged ischemia

Skeletal muscle dialysate NE levels decreased from 19 ± 4 pg/ml at control to 9 ± 4 pg/ml at 30 min of ischemia and reached 2 ± 0 pg/ml at 60 min of ischemia (Fig. 2). The decrease in dialysate NE level was maintained after 2 h of ischemia. Then skeletal muscle dialysate NE levels markedly increased to 143 ± 30 pg/ml at 4 h of ischemia. The dialysate NE levels continued to increase progressively and reached 289 ± 45 pg/ml at 6 h of ischemia. Skeletal muscle dialysate DHPG levels decreased from 38 ± 2 pg/ml at control to 5 ± 1 pg/ml at 2 h of ischemia and reached 7 ± 1 pg/ml at 6 h of ischemia.

3.2. Involvement of NE uptake$_1$ transport, Ca^{2+} channels and cytosol Ca^{2+} in dialysate NE levels during prolonged ischemia

Dialysate NE increases at 4 and 6 h-skeletal muscle ischemia were not suppressed by treatment with desipramine (Fig. 3). Dialysate NE increases at 4 and 6 h-skeletal muscle ischemia were not suppressed by treatment with ω-conotoxin GVIA. Treatment with TMB-8 significantly suppressed the dialysate NE increase at 4 h-skeletal muscle ischemia. But at 6 h-skeletal muscle ischemia, there was no significant difference in dialysate NE levels among treatments.

Table 1
Changes in heart rate (HR) and mean arterial pressure (MAP) in 6 h-hindlimb ischemia

	Control	2 h	4 h	6 h
HR (beats/min)	283 ± 10	292 ± 4	293 ± 8	302 ± 8*
MAP (mmHg)	104 ± 6	114 ± 3*	111 ± 4	108 ± 4

Values are means ± S.E. from six rabbits. Data were obtained during control, after 2, 4, and 6 h of hind limb ischemia.
* $P < 0.05$ vs. control.

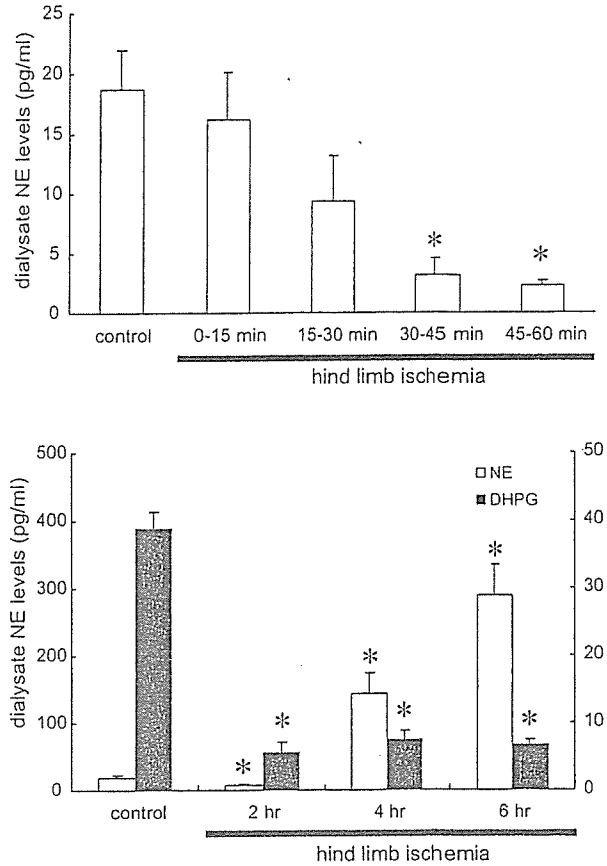

Fig. 2. (Upper panel) Time course of dialysate norepinephrine (NE) levels during 60 min-hind limb ischemia. Values are means ± S.E. ($n = 6$). *$P < 0.05$ vs. control value. (Lower panel) Time courses of dialysate NE and dihydroxyphenylglycol (DHPG) levels during 6 h-hind limb ischemia. Values are means ± S.E. ($n = 6$). *$P < 0.05$ vs. control value.

3.3. Time course of dialysate lactate levels during hind limb ischemia

Skeletal muscle dialysate lactate levels increased from 0.6 ± 0.07 nmol/l at control to 1.73 ± 0.17 nmol/l at 45–60 min

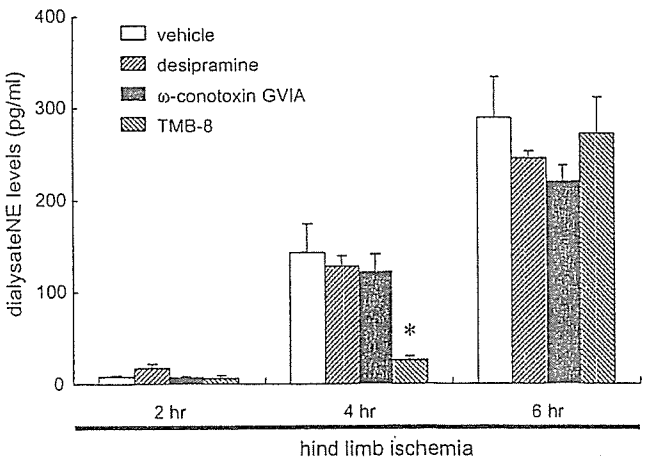

Fig. 3. Effects of pharmacological intervention on dialysate norepinephrine (NE) levels evoked by 6 h-hind limb ischemia. Desipramine (100 μM), ω-conotoxin (10 μM), or TMB-8 (1mM) was locally administered through the probe. Values are means ± S.E. ($n = 6$). *$P < 0.05$ vs. concurrent value of vehicle group.

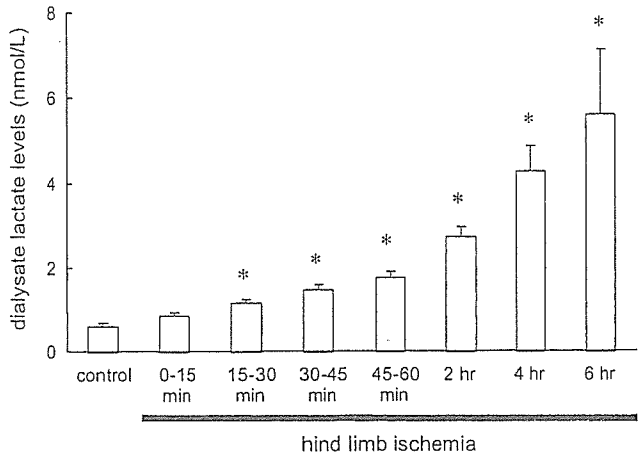

Fig. 4. Time course of dialysate lactate levels during 6 h-hind limb ischemia. Values are means ± S.E. ($n = 6$). $^*P < 0.05$ vs. control value.

of ischemia (Fig. 4). These step-wise increases were continued for 6 h of the hind limb ischemia.

4. Discussion

Using dialysis techniques in the in vivo rabbit skeletal muscle, we examined interstitial levels of NE in the control and ischemic period, and observed the biphasic response of dialysate NE in ischemic skeletal muscle. Ischemia induced an initial reduction followed by a progressive increment in dialysate NE levels. Here we discuss changes in interstitial NE and possible mechanisms underlying sympathetic nerve impairment.

Within 2 h of acute skeletal muscle ischemia, unlike acute myocardial ischemia, skeletal muscle interstitial NE levels continued to decline progressively, decreasing to one-tenth of control at 60 min of ischemia. A previous study demonstrated that skeletal muscle ischemia modulated the baroreflex control of regional muscle sympathetic activity (Cornett et al., 2000). At 75 min of acute skeletal muscle ischemia, hemodynamic responses to carotid occlusion were preserved while the interstitial NE response to carotid occlusion was blunted in the ischemic region (Tokunaga et al., 2003b). These results indicate that the systemic response to baroreflex remained intact while the skeletal muscle sympathetic response was impaired in ischemic regions. Earlier studies reported that acute limb ischemia reduced the conduction of motor nerves such as sciatic nerve (Fern and Harrison, 1994), and induced axonal degeneration histologically (Makitie and Teravainen, 1977; Nukada and Dyek, 1987). Axonal conduction in the ischemic muscle sympathetic nerve may be impaired as well as in sensory and motor nerves. In addition to diminished axonal conductance, the interstitial NE response to high K^+ but not tyramine was suppressed during the 75 min of acute skeletal muscle ischemia, although NE content at muscle sympathetic nerve endings was preserved during the ischemia (Tokunaga et al., 2003b). This result indicates that exocytotic NE releasing function in muscle sympathetic nerve endings might be suppressed during 75 min of acute skeletal muscle ischemia. Therefore, initial reduction of NE release may be mediated by an impairment of axonal conduction and/or NE releasing function.

After 2 h of acute skeletal muscle ischemia, skeletal muscle interstitial NE levels significantly increased and finally reached 20-fold that of control. This amount of NE release is higher than that evoked by baroreflex or high K^+. This level is similar to that evoked by the Na^+–K^+ ATPase inhibitor, ouabain (Tokunaga et al., 2003a). The amount of NE release evoked by ischemia may be dependent on the density of sympathetic innervation. Dispersed organ systems such as skeletal muscle have a thin and diffuse sympathetic innervation. This is the first report to describe that marked NE release is induced from muscle sympathetic nerve endings in the ischemic region after 2 h of skeletal muscle ischemia. Numerous histological changes of skeletal muscle have been reported after ischemia and reperfusion injury (Patterson and Klenerman, 1979; Turchányi et al., 2005). However, there is no histochemical evidence of the impaired sympathetic nerves in the skeletal muscle ischemia.

In the case of skeletal muscle ischemia, ω-conotoxin GVIA did not suppress NE efflux. N-type Ca^{2+} channels are not involved in this NE efflux. Desipramine did not alter NE efflux during skeletal muscle ischemia. Desipramine inhibits carrier-mediated NE transport in both directions. Considering that desipramine did not alter interstitial NE levels, the amounts of NE release and uptake via normal transport can be surmised to be negligible. Second, the increase in skeletal muscle interstitial NE levels was not associated with an increase in skeletal muscle interstitial DHPG levels, indicating that skeletal ischemia fails to induce axoplasmic NE elevation via alterations in monoamine activity, NE mobilization from stored vesicle, and NE uptake. Further, desipramine did not suppress NE efflux. These results exclude the possibility that marked increases in skeletal muscle interstitial NE could be due to carrier-mediated outward transport of NE for removal of elevated axoplasmic NE concentration. The membrane NE transporter exists in the skeletal muscle sympathetic nerve endings (Cabassi et al., 2001; Tokunaga et al., 2003a), but was not involved in outward transport of NE. Thus, we consider that a ω-conotoxin GVIA insensitive and desipramine-resistant NE release mechanism exists after 2 h of acute skeletal muscle ischemia.

TMB-8 significantly suppressed the marked NE release at 4 h of skeletal muscle ischemia. TMB-8 is well known to inhibit Ca^{2+} release from intracellular Ca^{2+} stores. TMB-8 inhibits caffeine-induced catecholamine release from perfused adrenal gland in the absence of extracellular Ca^{2+} (Yamada et al., 1988). Studies using chromaffin cells, brain slices and synaptosomes have suggested that metabolic inhibition induces intracellular Ca^{2+} overload (Milusheva et al., 1992), and a rise in the intracellular Ca^{2+} causes exocytotic catecholamine release without membrane depolarization (Dry et al., 1991; Du et al., 1997). Moreover, an in vitro study with adrenergic nerves of guinea-pig vas deferens suggested that Ca^{2+} release from intracellular Ca^{2+} stores is to some extent involved in the NE release evoked by elevation of intracellular Na^+ (Katsuragi et al., 1994). Under energy-depleted conditions, Ca^{2+} overload

in synaptosomes of noradrenergic neurons from the brain is an important mechanism for the enhanced release of neurotransmitter, with a reversal of Na^+–Ca^{2+} exchange possibly the key pathway leading to intraneuronal Ca^{2+} overload (Du et al., 1997). We consider that Ca^{2+} release from intracellular Ca^{2+} stores is partly involved in the NE release at 4 h of skeletal muscle ischemia.

At 6 h of skeletal ischemia, increment in dialysate NE level was not suppressed by the pretreatments. This result suggests that another mechanism may be involved in NE release, which is insensitive to desipramine, ω-conotoxin GVIA, and TMB-8. Alternatively, the NE release may occur with development of irreversible membrane damage and can no longer be inhibited by pharmacological interventions. Future work should concentrate on these aspects of NE release during the later period.

4.1. Methodological considerations

The limitation of this experiment is related to the methodology and the duration of the hind limb ischemia. In a variety of these experimental models for organ ischemia, we chose microsphere injection and iliac artery occlusion for the short and prolonged hind limb ischemia model. A preliminary experiment indicated that common iliac artery occlusion did not yield severe ischemia or muscle necrosis in a chronic ischemic model because collateral flow prevents skeletal muscle ischemia. The combination of artery occlusion and injection of microsphere was used for the hind limb ischemic model. In the hind limb ischemia, however, we did not measure skeletal muscle blood flow. To confirm whether this perturbation induced reduction of blood flow and tissue ischemia, we measured dialysate lactate levels in skeletal muscle as an index of tissue ischemia. This perturbation induced increases in dialysate lactate levels. In the present study, dialysate NE responses were examined in prolonged 6 h ischemia. Temporal changes in MAP and HR appeared but sustained significant hemodynamic changes were not observed. This duration was referred to the experiments on the tourniquet application and release time (Sapega et al., 1985; Mitrev et al., 1996). Four to 6 h of ischemic periods has been thought to produce extensive and reversible damage of skeletal muscle. Therefore, data on pharmacological intervention were obtained within 6 h of skeletal muscle ischemia.

Ischemia induced biphasic NE responses in the skeletal muscle. Initial reduction of NE release may be mediated by an impairment of axonal conduction and/or NE releasing function, while in the later phase, the skeletal muscle ischemia-induced NE release was partly attributable to exocytosis via intracellular Ca^{2+} overload rather than opening of calcium channels or carrier mediated outward transport of NE.

Acknowledgements

This study was supported by Grants-in Aid for scientific research (15590787) from the Ministry of Education, Culture, Sports, Science and Technology; the Research Grants for Cardiovascular Disease (H13C-1) from the Ministry of Health, Labor and Welfare.

References

Akiyama, T., Yamazaki, T., Ninomiya, I., 1991. In vivo monitoring of myocardial interstitial norepinephrine by dialysis technique. Am. J. Physiol. 261, H1643–H1647.

Akiyama, T., Yamazaki, T., Ninomiya, I., 1993. Differential regional responses of myocardial interstitial noradrenaline levels to coronary occlusion. Cardiovasc. Res. 27, 817–822.

Akiyama, T., Yamazaki, T., 2001. Myocardial interstitial norepinephrine and dihydroxyphenylglycol levels during ischemia and reperfusion. Cardiovasc. Res. 49, 78–85.

Anton, A.H., Sayer, D.F., 1962. A study of the factors affecting the aluminum oxide-trihydroxyindole procedure for the analysis of catecholamine. J. Pharmacol. Exp. Ther. 138, 360–375.

Barker, D., Saito, M., 1981. Autonomic innervation of receptors and muscle fibers in cat skeletal muscle. Proc. Roy. Soc. Lond., B: Biol. Sci. 212, 317–332.

Cabassi, A., Vinci, S., Quartieri, F., Moschini, L., Borghetti, A., 2001. Norepinephrine uptake is impaired in skeletal muscle of hypertensive rats in vivo. Hypertension 37, 698–702.

Ciuffo, A.A., Ouyang, P., Becker, L.C., Levin, L., Weisfeldt, M.L., 1985. Reduction of sympathetic inotropic response after ischemia in dogs. Contributor to stunned myocardium. J. Clin. Invest. 75, 1504–1509.

Cornett, J.A., Herr, M.D., Gray, K.S., Smith, M.B., Yang, Q.X., Sinoway, L.I., 2000. Ischemic exercise and the muscle metaboreflex. J. Appl. Physiol. 89, 1432–1436.

Cui, J., Wilson, T.E., Shibasaki, M., Hodges, N.A., Grandall, C.G., 2001. Baroreflex modulation of muscle sympathetic nerve activity during postgrip muscle ischemia in human. J. Appl. Physiol. 91, 1679–1686.

Dry, K.L., Phillips, J.H., Dart, A.M., 1991. Catecholamine release from bovine adrenal chromaffin cells during anoxia or metabolic inhibition. Circ. Res. 69, 466–474.

Du, X.-J., Bobik, A., Little, P.J., Esler, M.D., Dart, A.M., 1997. Role of Ca^{2+} in metabolic inhibition-induced norepinephrine release in rat brain synaptosomes. Circ. Res. 80, 179–188.

Fagius, J., Berne, C., 1994. Increase in muscle sympathetic activity in humans after food intake. Clin. Sci. (London) 86, 159–167.

Fern, R., Harrison, P.J., 1994. The relationship between ischaemic conduction failure and conduction velocity in cat myelinated axons. Exp. Physiol. 79, 571–581.

Fujii, T., Kurata, H., Takaoka, M., Muraoka, T., Fujisawa, Y., Shokoji, T., Nishiyama, A., Abe, Y., Matsumura, Y., 2003. The role of renal sympathetic nervous system in the pathogenesis of ischemic acute renal failure. Eur. J. Pharmacol. 481, 241–248.

Hill, J.M., Adreani, C.M., Kaufman, M.P., 1996. Muscle reflex stimulates sympathetic postganglionic efferents innervating triceps surae muscle of cats. Am. J. Physiol. 271, H38–H43.

Idström, J.-P., Soussi, B., Elander, A., Bylund-Fellenius, A.-C., 1990. Purine metabolism after in vivo ischemia and reperfusion in rat skeletal muscle. Am. J. Physiol. 258, H1668–H1673.

Katsuragi, T., Ogawa, S., Furukawa, T., 1994. Contribution of intra- and extracellular Ca^{2+} to noradrenaline exocytosis induced by ouabain and monensin from guinea-pig vas deferens. Br. J. Pharmacol. 113, 795–800.

Kawada, T., Yamazaki, T., Akiyama, T., Sato, T., Shishido, T., Inagaki, M., Tetewaki, T., Yanagiya, Y., Sugimachi, M., Sunagawa, K., 2000. Cyanide intoxication induced exocytotic epinephrine release in rabbit myocardium. J. Auton. Nerv. Syst. 80, 137–141.

Lindsay, T.F., Liauw, S., Romaschin, A.D., Walker, P.M., 1990. The effect of ischemia/reperfusion on adenine nucleotide metabolism and xanthine oxidase production in skeletal muscle. J. Vasc. Surg. 12, 8–15.

Mair, J., 1999. Tissue release of cardiac markers: from physiology to clinical applications. Clin. Chem. Lab. Med. 37, 1077–1084.

Makitie, J., Teravainen, H., 1977. Peripheral nerve injury and recovery after temporary ischemia. Acta Neuropathol. (Berl.) 37, 55–63.

Milusheva, E., Doda, M., Pasztor, E., Lajtha, A., Sershen, H., Vizi, E.S., 1992. Regulatory interactions among axonal terminals affecting the release of different transmitters from rat striatal slices under hypoxic and hypoglycemic conditions. J. Neurochem. 59, 946–952.

Mitrev, Z., Ihnken, K., Poloczek, Y., Hallmann, R., Herold, H., Unkelbach, U., Zimmer, G., Freisleben, H.J., Beyersdorf, S., Beyersdorf, F., 1996. Controlled reperfusion of the extremities for preventing local and systemic damage after prolonged ischemia. An experimental study with the swine model. Zentralbl. Chir. 121, 774–787.

Nukada, H., Dyek, P.J., 1987. Acute ischemia causes axonal stasis, swelling, attenuation and secondary demyelination. Ann. Neurol. 22, 311–318.

Patterson, S., Klenerman, 1979. The effect of pneumatic tourniquets on the ultrastructure of skeletal muscle. J. Bone Joint Surg. Br. 61, 178–183.

Schömig, A., Dart, A.M., Dietz, R., Mayer, E., Kubler, W., 1984. Release of endogenous catecholamines in the ischemic myocardium of the rat. Part A. Locally mediated release. Circ. Res. 55, 689–701.

Schömig, A., Fischer, S., Kurz, T., Richardt, G., Schömig, E., 1987. Non-exocytotic release of endogenous noradrenaline in the ischemic and anoxic rat heart: mechanism and metabolic requirements. Circ. Res. 60, 194–205.

Sapega, A.A., Heppenstall, R.B., Chance, B., Park, Y.S., Sokolow, D., 1985. Optimizing tourniquet application and release times in extremity surgery. A biochemical and ultrastructual study. J. Bone Joint Surg. Am. 67, 303–314.

Tanaka, E., Hattan, N., Ando, K., Ueno, H., Sugio, Y., Mohammed, M.U., Voltchikhina, S.A., Mori, H., 2000. Amelioration of microvascular myocardial ischemia by gene transfer of vascular endothelial growth factor in rabbits. J. Thorac. Cardiovasc. Surg. 120, 720–728.

Thompson, L.P., Mohrman, D.E., 1983. Blood flow and oxygen consumption in skeletal muscle during sympathetic stimulation. Am. J. Physiol. 245, H66–H71.

Tokunaga, N., Yamazaki, T., Akiyama, T., Sano, S., Mori, H., 2003a. In vivo monitoring of norepinephrine and its metabolites in skeletal muscle. Neurochem. Int. 43, 573–580.

Tokunaga, N., Yamazaki, T., Akiyama, T., Sano, S., Mori, H., 2003b. Acute limb ischemia does not facilitate but inhibits norepinephrine release from sympathetic nerve endings in anesthetized rabbit. J. Cardiovasc. Pharmacol. 42, S7–S10.

Toyohara, T., Nada, O., Ikeda, K., 1986. Influence of ischemia on noradrenergic nerves in the terminal colon of humans and rats. Eur. Surg. Res. 18, 349–355.

Turchányi, B., Tóth, B., Rácz, I., Vendégh, Z., Fűrész, J., Hamar, J., 2005. Ischemia reperfusion injury of the skeletal muscle after selective deafferentation. Physiol. Res. 54, 25–31.

Welsh, D.G., Lindinger, M.I., 1993. Energy metabolism and adenine nucleotide degradation in twitch-stimulated rat hindlimb during ischemia-reperfusion. Am. J. Physiol. 264, E655–E661.

Yamada, Y., Teraoka, H., Nakazato, Y., Ohga, A., 1988. Intracellular Ca^{2+} antagonist TMB-8 blocks catecholamine secretion evoked by caffeine and acetylcholine from perfused cat adrenal glands in the absence of extracellular Ca^{2+}. Neurosci. Lett. 90, 338–342.

The EMBO Journal (2006) 25, 2889–2897 | © 2006 European Molecular Biology Organization | All Rights Reserved 0261-4189/06
www.embojournal.org

THE EMBO JOURNAL

Endophilin BAR domain drives membrane curvature by two newly identified structure-based mechanisms

Michitaka Masuda[1,4], Soichi Takeda[2,3,4], Manami Sone[1], Takashi Ohki[1], Hidezo Mori[2], Yuji Kamioka[1] and Naoki Mochizuki[1,*]

[1]Department of Structural Analysis, National Cardiovascular Center Research Institute, Suita, Osaka, Japan, [2]Department of Cardiac Physiology, National Cardiovascular Center Research Institute, Suita, Osaka, Japan and [3]Laboratory of structural biochemistry, RIKEN Harima Institute at SPring-8, Mikazuki-cho, Sayo, Hyogo, Japan

The crescent-shaped BAR (Bin/Amphiphysin/Rvs-homology) domain dimer is a versatile protein module that senses and generates positive membrane curvature. The BAR domain dimer of human endophilin-A1, solved at 3.1 Å, has a unique structure consisting of a pair of helix–loop appendages sprouting out from the crescent. The appendage's short helices form a hydrophobic ridge, which runs across the concave surface at its center. Examining liposome binding and tubulation *in vitro* using purified BAR domain and its mutants indicated that the ridge penetrates into the membrane bilayer and enhances liposome tubulation. BAR domain-expressing cells exhibited marked plasma membrane tubulation *in vivo*. Furthermore, a swinging-arm mutant lost liposome tubulation activity yet retaining liposome binding. These data suggested that the rigid crescent dimer shape is crucial for the tubulation. We here propose that the BAR domain drives membrane curvature by coordinate action of the crescent's scaffold mechanism and the ridge's membrane insertion in addition to membrane binding via amino-terminal amphipathic helix.

The EMBO Journal (2006) 25, 2889–2897. doi:10.1038/sj.emboj.7601176; Published online 8 June 2006
Subject Categories: membranes & transport; structural biology
Keywords: BAR domain; endophilin; liposome; membrane curvature; membrane insertion

Introduction

Membrane dynamics in a cell, such as membrane budding, tubulation, fission and fusion, is associated with changes in membrane curvature. The crystal structure of amphiphysin BAR (Bin/Amphiphysin/Rvs-homology) domain revealed an unexpected structural identity with arfaptin2, a binding protein to Arf and Rac small GTPases (Tarricone *et al*, 2001), and provided a common structural base for the sensing and the formation of positive curvature membrane by BAR-family proteins (Peter *et al*, 2004).

Endophilins are cytoplasmic proteins containing an N-terminal BAR domain and a C-terminal SH3 domain, and are involved in membrane dynamics (Schuske *et al*, 2003; Galli and Haucke, 2004; Wenk and De Camilli, 2004). There are five endophilin genes in the mammalian genomes, endophilin A1–3 and B1–2. Both A and B types are highly conserved from nematode to human. The most extensively studied one is endophilin-A1, a brain specific protein involved in clathrin-mediated synaptic vesicle endocytosis (Ringstad *et al*, 1997, 2001). Via SH3 domain, endophilins bind to the GTPase dynamin, a membrane scissor, and the polyphosphoinositide phosphatase synaptojanin, a clathrin-uncoater (Ringstad *et al*, 1997; de Heuvel *et al*, 1997; Verstreken *et al*, 2003). The BAR domain of endophilins is classified into the N-BAR subgroup characterized by a short amphipathic helical sequence preceding the consensus BAR-domain sequence (Peter *et al*, 2004). The N-BAR domain of endophilin-A1 binds to liposomes and induces the tubulation *in vitro*, requiring the short amphipathic helical sequence (Farsad *et al*, 2001).

The crescent-shaped BAR dimer structure implies a simple model to drive membrane curvature: the dimer may impress its positively charged concave surface on the negatively charged membrane to form a high-curvature membrane domain (Gallop and McMahon, 2005; McMahon and Gallop, 2005). This curvature-impressing or scaffold mechanism for membrane deformation is based on an assumption that the dimer behaves as a rigid body on the membrane (Zimmerberg and Kozlov, 2006). Although the essential requirement of positively charged residues on the concave surface has been suggested (McMahon and Mills, 2004; Peter *et al*, 2004), there have been no experimental supports for the scaffold mechanism. Here, we show the requirement of the molecular rigidity of the BAR dimer for membrane curvature on the basis of structure-oriented mutational analysis.

By determining the structure of endophilin-A1 BAR domain, we found a distinction from those of the known BAR domains: a helix–loop appendage of 30 amino acids stretch is inserted into the helix I of the canonical BAR domain. A pair of the helices of the appendages forms a hydrophobic ridge, which runs across the center of the concave surface of the dimer. We analyzed the function of this ridge as well as the previously proposed structure, the N-terminal amphipathic helix and the crescent main body, for membrane deformation (Peter *et al*, 2004). N-terminal amphipathic helix is essential for membrane binding. The crescent main body of the BAR dimer is required for impressing its intrinsic curvature to the membrane. The ridge contributes to deform the membrane

*Corresponding author. Department of Structural Analysis, National Cardiovascular Center Research Institute, 5-7-1 Fujishiro-dai, Suita, Osaka 565-8565, Japan. Tel.: +81 6 6833 5012; Fax: +81 6 6835 5461; E-mail: nmochizu@ri.ncvc.go.jp
[4]These authors contributed equally to this work

Received: 15 November 2005; accepted: 8 May 2006; published online: 8 June 2006

presumably by penetrating into the membrane. Our results illustrate how these three components coordinate to induce membrane deformation.

Results

Endophilin-A1 BAR domain has a unique appendage

The structure of the BAR domain of human endophilin-A1 (amino acid 1–247, hereafter EndA1-BAR) was solved at 3.1 Å resolution by a multi-wavelength anomalous dispersion method. The structure of EndA1-BAR dimer is similar to that of amphiphysin (Peter *et al*, 2004) and arfaptin2 (Tarricone *et al*, 2001): a crescent-shaped dimer composed of a 6-helix bundle core and two 3-helix bundle arms extended from the core (Figure 1A). The whole structure of EndA1-BAR dimer can be precisely superimposed on that of amphiphysin and arfaptin (Figure 1B). All three structures show nearly identical dimer shapes. Notably, the present EndA1-BAR structure from a tetragonal crystal packing is almost completely the same as an independent crystal structure from an orthogonal crystal packing (Supplementary Figure 1; and Weissenhorn, 2005). The RMS deviations are 0.63, 0.86 and 0.80 Å for Cα atoms in monomers A, B and dimer, respectively. The structural identity indicates that the crescent shape is stably present in solution. Consistent with previous results (Habermann, 2004; Peter *et al*, 2004), structure-based sequence alignment reveals that these three proteins are poorly conserved in amino-acid sequence including the residues possibly important for the crescent-shape formation (Supplementary Figure 2).

We find a unique structure of the EndA1-BAR, an appendage-like structure protruded from the center of the dimer (Figure 1A). The sequence alignments of the BAR-family proteins indicated that this appendage appears unique to the endophilin-family proteins including nadrin (Habermann, 2004; Peter *et al*, 2004) and the candidates from yeasts (Supplementary Figure 2). The appendage (Q59–Q88) has an N-terminal short helix and a loop of which electron density is mostly missing (N72–G85). The pair of helices appears to stay on the main body and forms a ridge across the center of the concave dimer surface. The helix displays, on its top surface, a series of hydrophobic residues (P62, A63, A66 and M70) aligned 60° against the longitudinal axis of the dimer (Figure 1C). Other than the conserved hydrophobic amino acids of the ridge, the appendage sequences show clear distinction between endophilin-A and endophilin-B (Supplementary Figure 2). The B type endophilins show cytoplasmic localization, presumably being involved in intracellular membrane dynamics (Farsad *et al*, 2001; Modregger *et al*, 2003; Karbowski *et al*, 2004). Analyses of chimeric mutations in the appendage between EndA1-BAR and EndB1-BAR suggest that BAR domain may contribute to defining where to target, plasma membrane or intracellular organ membrane (Supplementary Figure 3).

The appendage's penetration enhances liposome tubulation

To investigate the functional significance of the hydrophobic ridge of the endophilin-specific appendage, we first examined the effects of point mutations in this region (red residues in Figure 1C) on the liposome binding and tubulation activities *in vitro* (Figures 2A and 3). Introduction of membrane-repulsive negative charge (A66D) lost the ability to form tubes from liposomes. Hydrophilic mutations (A63S/A66S (SS) and A63S/A66S/M70Q (SSQ)) reduced the number of tubes (<1/100) and induced three-time enlargement of the tube diameter. In contrast, a bulky hydrophobic residue

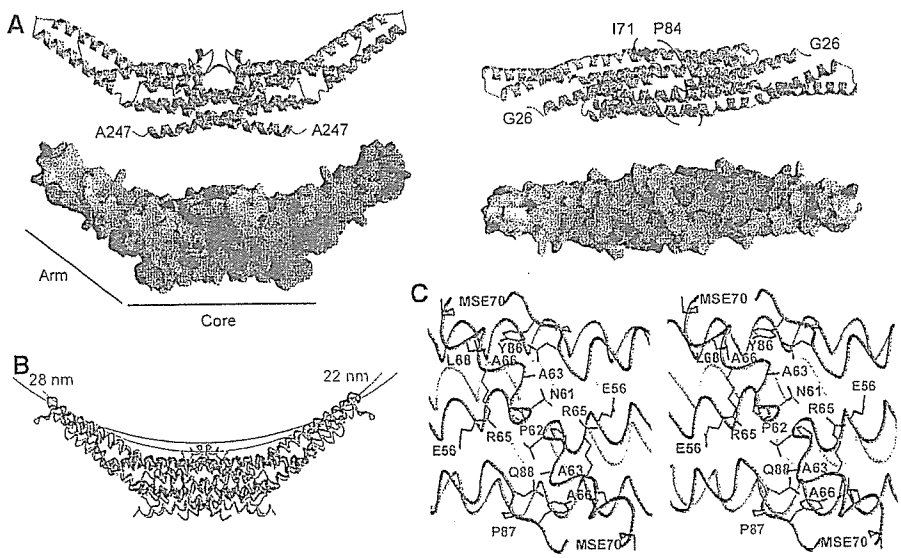

Figure 1 Structure of human endophilin-A1 BAR domain dimer. (A) Ribbon representation (a green monomer with a red appendage and a pale-blue monomer with a blue appendage) and surface electrostatic potential (red, $-15\,kTe^{-1}$; blue, $15\,kTe^{-1}$) of the dimer viewed from the side (left) and from the top (right). The numbered amino-acid residues are the first and the last ones in consecutive polypeptide segments determined in this model. (B) Comparison of three BAR domain structures in trace representation. Red, endophilin-A1 (PDB ID: 1X03); green, amphiphysin (1URU); blue, arfaptin2 (1I4D). The red and green arcs with indicated diameters represent curved membranes fit the concave surface of endophilin-A1 and amphiphysin, respectively. (C) Stereo view of the appendages. Side-chains of the residues forming the hydrophobic ridge and those of interacting with residues of the main body are shown.

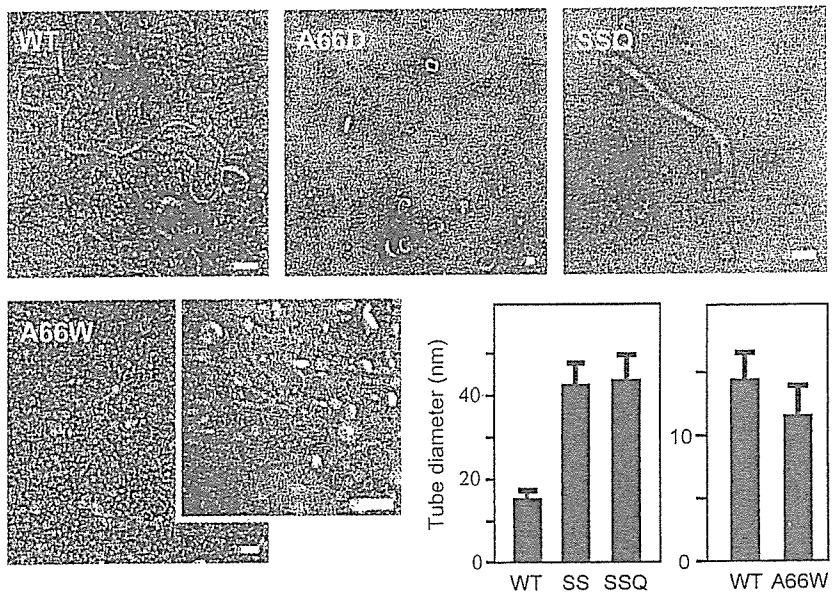

Figure 2 Liposome tubulation by endophilin-A1 BAR domains with mutations in the hydrophobic ridge. WT, 7 μM wild-type BAR domain incubated for 10 min; A66D, 28 μM, 10 min; SSQ, A63S/A66S/M70Q triple mutant, 28 μM, 10 min; A66W, 1.4 μM, 10 min (vesiculated, left panel) and 10 s (tubulated, right panel). Tubulation was not observed when incubated for longer than 1 min. Scale, 100 nm. The bar graphs show tubule diameter (mean and s.d.). SS, A63S/A66S double mutant, 28 μM, 10 min.

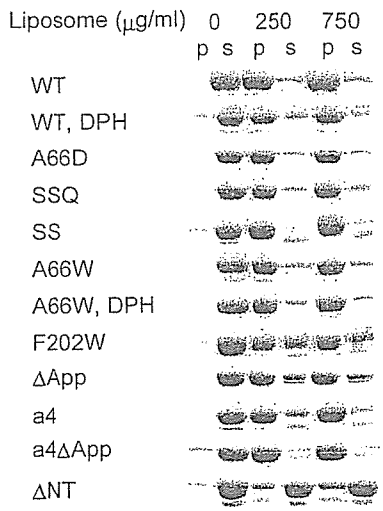

Figure 3 Liposome binding assays of endophilin-A1 BAR domain and its mutants. Protein (200 μg/ml) was co-sedimented with liposomes (0, 250 and 750 μg/ml). Proteins recovered from the pellet (p) and the supernatant (s) were analyzed by SDS–PAGE. The DPH-liposomes show similar binding capacity for the wild type (WT) and the A66W mutants. The liposome binding activity is slightly reduced in the F202W and the appendage-less mutants (ΔApp) and is almost lost in the helix 0 truncated mutant (ΔNT).

(A66W) led to extensive vesiculation and less tubulation. All these mutations did not affect the liposome binding. These results suggest an important role for the hydrophobic ridge in the membrane curvature formation but not in the membrane binding.

Although the ridge reduces the intrinsic curvature of the concave surface (red line in Figure 1B), it appears to promote the membrane curvature formation with conserved hydrophobicity. This raises the possibility that the ridge penetrates into the membrane when the concave surface makes tight contact with the membrane. This possibility was investigated using tryptophan fluorescence, which is sensitive to hydrophobicity of the microenvironment around the indole moiety. The A66W mutant showed 10-nm blueshift of the fluorescence peak in a liposome-dose-dependent and saturable manner, while F202W, a control mutant in which Phe202 on the convex surface was mutated to Trp, did not show any shift (Figure 4A and Supplementary Figure 5). The amount of the blueshift was greater than that observed in 50% DMSO or 50% methanol, indicating that the indol moiety was in a highly hydrophobic environment.

To determine whether this blueshift was caused by the insertion of the indol moiety into the hydrophobic core of the lipid bilayer, we made fluorescence resonance energy transfer (FRET) assays using diphenyl-hexatriene (DPH) as the acceptor probe. DPH has been shown to insert specifically in the nonpolar interior of the membrane and not to alter the membrane structure and dynamics (Repáková *et al*, 2005). DPH liposomes did not affect liposome binding and tubulation (Figure 3 and Supplementary Figure 4). A66W but not F202W showed effective FRET from the 340-nm tryptophan fluorescence (donar) to the DPH fluorescence (acceptor) peaked at 430 nm (Figure 4B and C). It was not caused by changes in the fluorescence property of DPH itself possibly accompanied by tubulation/vesiculation of liposomes (Figure 4D and Supplementary Figure 6). These data suggest that the indol ring of 66W penetrates into the hydrophobic core of the membrane and that the remaining residues of the ridge, about 8 Å in height, appear to be embedded in the layer of lipid head-groups of the contacting membrane leaflet. These results confirmed that the ridge is contacting membrane and that the convex is not contacting membrane surface.

To provide further support for the membrane insertion of the ridge in the wild-type EndA1-BAR, we made a mutant

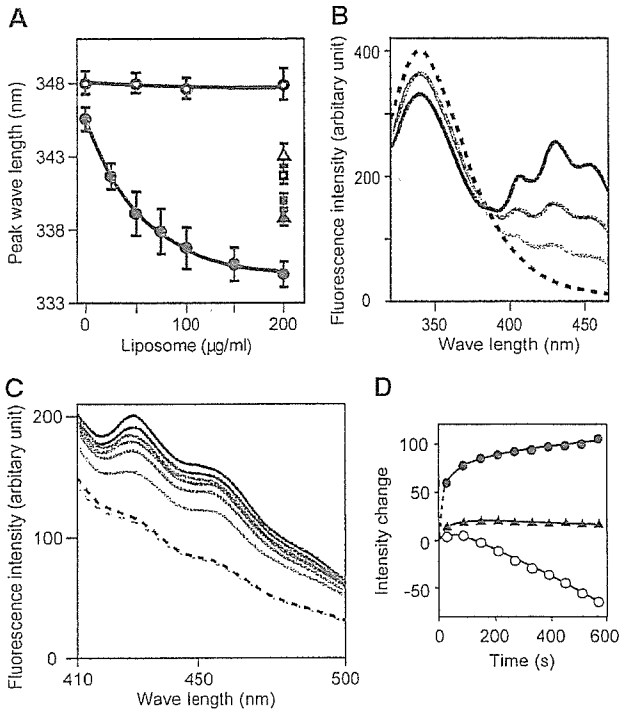

Figure 4 Tryptophan fluorescence blueshift and FRET assays. (**A**) Tryptophan fluorescence emission peak when excited at 280 nm was observed in different concentration of liposome. A66W (●), F202W control mutant (○), A66W alone in 50% DMSO (▲), in 50% MeOH (■), F202W alone in 50% DMSO (△), in 50% MeOH (□), 140 μg/ml protein for all measurements. Mean and s.d. ($N = 4$–11). The dose dependency is significant ($P \ll 0.001$) for the A66W mutant but insignificant ($P > 0.8$) for the F202W mutant (one-way ANOVA). DMSO and MeOH were used as blueshift inducer for tryptophan. (**B**) Dose-dependent FRET efficiency from the A66W tryptophan to DPH incorporated in liposomes was examined by the changes of fluorescence. Fluorescence spectrum of A66W (100 μg/ml) with the control liposome (200 μg/ml) excited at 280 nm (hatched). Pale to dark solid curves represent DPH:lipid weight ratios of 1:2000, 1:1000 and 1:500 in the same condition. (**C**) Time-dependent increase in the FRET efficiency from either A66W (pale to dark solid lines, from 30 to 570 s) or F202W tryptophan (pale and dark hatched lines, at 30 and 570 s) to DPH incorporated in liposomes. DPH:lipid weight ratio is 1:500. (**D**) The intensity changes at the 430-nm peak are plotted against time. A66W (●), F202W (▲) excited at 280 nm and A66W (○) excited at 360 nm.

with amphiphysin/arfaptin shape and examined its tubulation activity. The mutant (ΔApp), in which the entire appendage (Q59–Q88) was replaced with a helical stretch (AHLSSLLQ) derived from arfaptin2 sequence (A152–Q159, Y155S), show the crystal structure of a canonical BAR-domain dimer as designed (Figure 5A and Supplementary Figure 7). The ΔApp could bind to liposomes (Figure 3) and cause tubulation to a lesser extent than the wild type and amphiphysin-BAR (Figure 5D and Supplementary Figure 4). As the diameter of the tubules reflects the membrane curvature if the section of the tube is circle, we measured the diameter of the tube to compare the curvature of the EndA1-BAR and its mutant-induced tubes. Despite the higher curvature of the concave surface, the ΔApp dimer induced larger diameter tubules than the wild type did, indicating a positive contribution of the wild-type hydrophobic ridge to drive membrane curvature. Taken all together, the hydrophobic ridge penetrates into the interfacial leaflet of the lipid bilayer when the concave surface is in contact with the membrane and promotes membrane curvature formation.

The BAR domain is rigid enough to impose its intrinsic curvature on membrane

A simple model for the concave surface-driven mechanism is that each BAR domain dimer acts as a molecular mold that impresses its curved surface on the membrane. This model suggests that the membrane curvature approximately mirrors the curvature of the concave surface. Indeed, the diameters of tubules induced by amphiphysin, ΔApp (Figure 5D), SS and SSQ mutants (Figure 2) are compatible with the model-based prediction (see Supplementary Table II for statistical analysis). However, this model has an assumption that the dimer should be rigid enough to overcome the bending resistance of the membrane (Nossal and Zimmerberg, 2002; Farsad and De Camilli, 2003). To examine whether the molecular mold mechanism is feasible, we developed a straight BAR domain by inserting one helical pitch into the helix II in the proximal portion of the extending arm (QSAL is inserted between I154 and Q155). This mutation (a4) would compensate the unequal lengths between helix II and III in the arm, a common feature of the known BAR domain structures, and let the curved arm into a straight one. Although the a4 mutant was designed simply to straighten the curvature of the domain, the structure solved at 2.4 Å resolution shows that it actually has the very interesting property of a flexible arm rather than a rigid one (Figure 5B). Four monomers in the asymmetrical unit show deviation in the bending angles of arms. The blue and the green monomers have straight arms while the orange monomer shows a bending pattern similar to the wild type and the yellow monomer is an intermediate. The structural deviation almost exclusively occurs in the helix kink regions (Supplementary Figure 8), indicating that the arm can swing at least from the bend-free straight position to nearly the wild-type position.

The a4 mutant allowed us to examine how flexibility of the crescent-shaped main body of the BAR dimer affects the membrane curvature formation. The insertion of one helical pitch slightly distorts relative position of the helix II and III (Figure 5C), but does not largely rearrange the spatial positions of the residues on the concave surface of the arm (Supplementary Figure 8). Indeed, the a4 mutant and its appendage-lacking derivative (a4ΔApp) retained normal liposome binding activity (Figure 3). The a4 mutant vesiculated liposomes without any tubulation, while a4ΔApp lost these membrane-deforming activities (Figure 5D and Supplementary Figure 4). The concave surface-induced membrane deforming activity appeared to be lost in the a4 mutant, while the appendage's membrane insertion remained active. These results suggested that the rigidity of the crescent dimer structure is essential for liposome tubulation but not for vesiculation, although appendage insertion induces the vesiclulation.

Roles for the amphipathic helix 0 of the N-BAR domain

The structure of a short amphipathic helix (helix 0) characterizing the N-BAR (Peter *et al*, 2004) can be resolved in the a4 mutant structure due to its tight crystal packing (Figures 5B and 6). The helix 0 is disordered in the wild type (Figure 6) and the ΔApp structures. The helix 0 has been

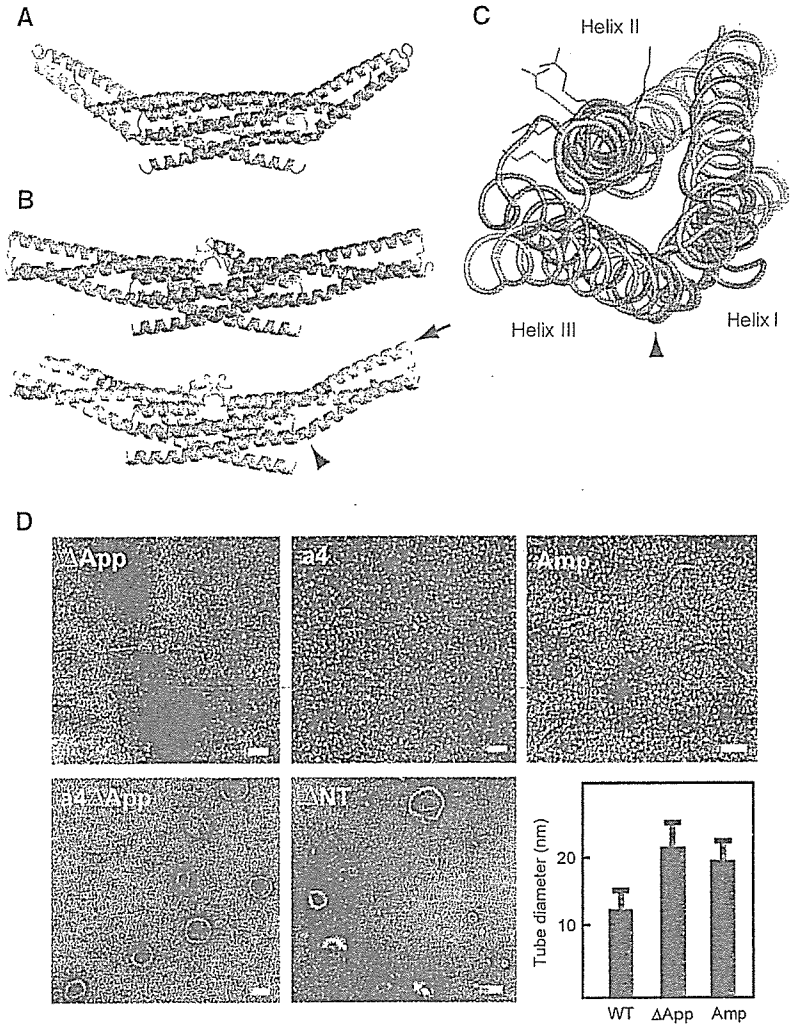

Figure 5 Distinct liposome tubulation induced by endophilin-A1 BAR domain mutants. (A) Ribbon representation of a mutated EndA1-BAR dimer lacking the entire appendages (ΔApp, PDB ID: 1X04). The entire appendage (Q59–Q88) was replaced with a helical stretch (AHLSSLLQ) derived from arfaptin2 sequence (A152–Q159, Y155S). Red, mutated segment. (B) Ribbon representation of the a4 mutant with swinging arms (PDB ID: 2D4C). One helical pitch was inserted into the helix II in the proximal portion of the extending arm (QSAL was inserted between I154 and Q155). Two dimers in the asymmetrical unit are shown separately. Red, inserted segment; magenta, helix 0. The bending patterns of the helix II and III varies among four monomers. An obvious kink in the helix III remains in the orange monomer (arrowhead, also in (C)). The residual curvature in the blue–green dimer is provided by the intersection of the monomers. (C) Superimposition of the a4 mutant monomer (orange one in (B)) and the wild-type monomer (blue) in the core region. A view from the distal end along the helix II (arrow in (B)) shows the maximum structural difference in these arms. Side chains of K171, 173 and R174 are shown. The helix III rotates 12° counterclockwise and shift 6 Å relative to the helix II at the distal end of the arm. The helix 0 and the core region are omitted. (D) Negatively stained liposome tubules induced by the BAR domains of endophilin mutants and amphiphysin. ΔApp, 7 μM, incubated for 10 min; a4, 7 μM, 10 min; a4ΔApp, 28 μM, 10 min; ΔNT, 21 μM, 10 min; Amp, 7 μM, 10 min. Note that a4, a4ΔApp, and ΔNT do not induce liposome tubulation. Scale, 100 nm. The bar graph shows tubule diameter (mean and s.d.).

suggested to be helical only when the amphiphysin BAR domain binds to liposomes (Peter *et al*, 2004). The helix 0 displays the hydrophobic branch of T14, V17 and V21 on one side, while K12, K16 and E19 on the other side (Figure 6). The helix 0 is connecting with the Helix I by a flexible linker G23–G24–A25. Consistent with the previous report (Farsad *et al*, 2001), truncation of the helix 0 (ΔNT) resulted in loss of liposome binding activity (Figure 3) and consequently abolished the tubulation (Figure 5D). In contrast, all the helix 0-containing mutants, including the A66D and the a4ΔApp showed intact liposome binding activity irrespective of their tubulation or vesiculation activities. These results indicate that the helix 0 in the endA1-BAR is critical for liposome binding and that the membrane binding of endA1-BAR via helix 0 is not sufficient to induce tubulation or vesiculation.

BAR domain induces tubular membrane deformation in vivo

To explore the significance of the helix 0, the rigid crescent mold, and the appendage of endophilin-A1 BAR domain *in vivo*, we further examined the membrane deformation activity of endophilin-A1 BAR domain in cells (Figure 7). Human umbirical vascular endothelial cells (HUVECs) expressing endophilin-A1 lacking SH3 domain (residues 1–296, hereafter, EndA1-BAR296), which was C-terminally tagged with enhanced green fluorescence protein (EGFP), exhibited intracellular fibrous structure similar to those induced by other BAR domain-containing molecules (Kamioka *et al*, 2004; Itoh *et al*, 2005). Notably, these structures developed from the periphery toward the center of the cells dynamically and disappeared reversibly in living cells (Figure 7E and

Supplementary Movie 1). Furthermore, these GFP-marked structures were co-localized with *in vivo* biotin-labeled membrane (Figure 7D), indicating that EndA1-BAR296-induced fibrous structure seems to be a membrane invagination originated from the plasma membrane. These structures were found in other cells we tested (Figure 7C). In clear contrast, ΔApp, ΔNT and a4 were incapable of inducing membrane deformation in cells, indicating the importance of helix 0, the rigid crescent shape, and the appendage of BAR domain for membrane deformation *in vivo*.

Discussion

The endophilin-A1 BAR domain dimer consists of three sub-modules: the crescent-shaped main body, the helix 0 and the unique appendage. We tried to understand the functional roles for these sub-modules in the membrane curvature formation. In this study by determining the structure of endopholin-A1 BAR domain and developing mutants that were critical for the sub-module structure, we have explored the roles of sub-modules.

Here, we show that the structural rigidity of the crescent-shaped main body is critical for membrane tubulation. The BAR dimer is sufficiently rigid to overcome the bending resistance of the membrane and to be scaffolds for the tubulation (McMahon and Gallop, 2005; Zimmerberg and Kozlov, 2006). The insertion of one helical-pitch into the helix II at distal to the kink brings flexibility to the dimer (a4 mutant). The relative position of the three helices in the

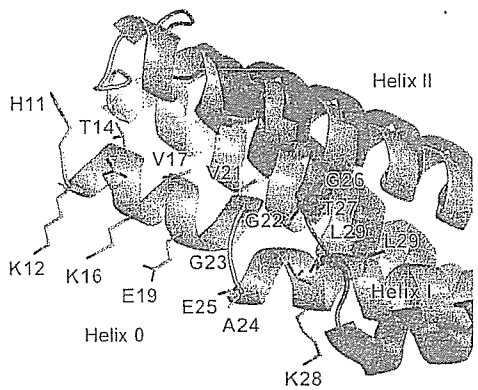

Figure 6 Close-up of helix 0 in an a4 mutant monomer (orange). The same superimposition as in Figure 5C but viewed from the side and displays the helix 0. The helix 0 is disordered in the wild-type structure (blue). The side chains of N-terminal residues are shown (H11KATQKVSEKVGGAEGTKL29 in the a4 and G26TKL in the wild type). The amphipathic helix 0 is stabilized by hydrophobic interactions with the helix II and III and also by hydrogen bonds with a symmetrical molecule.

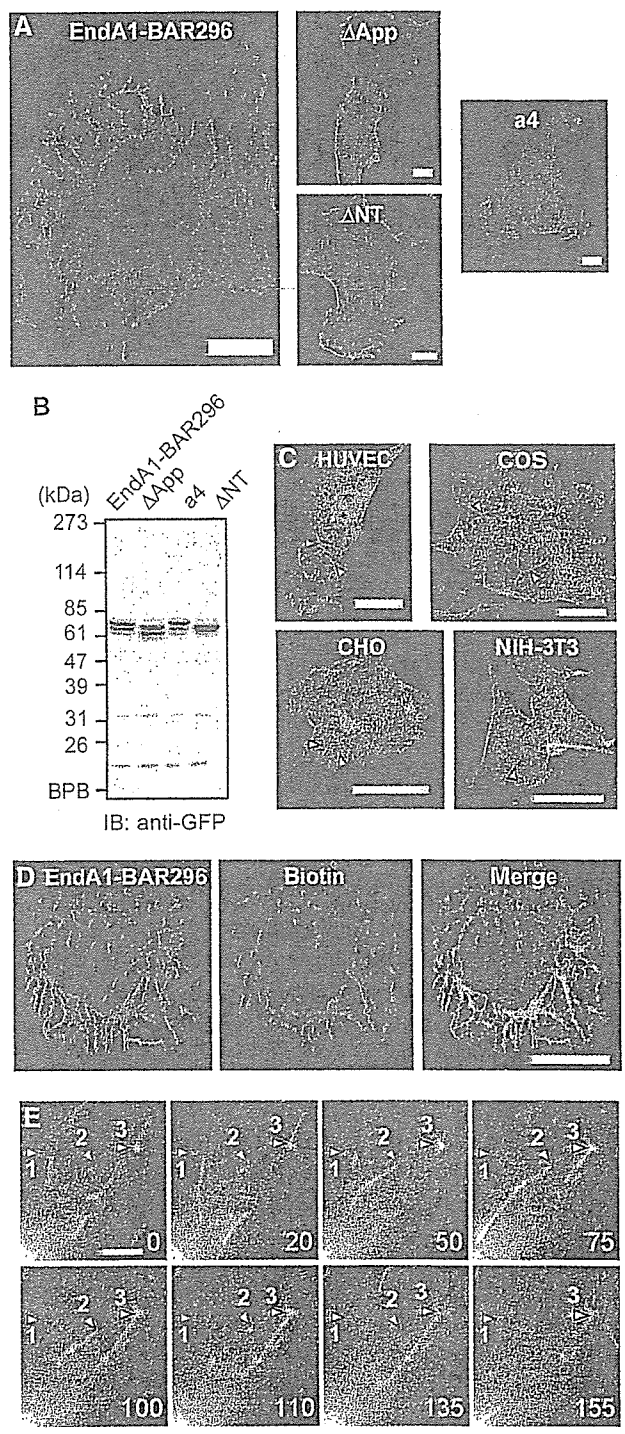

Figure 7 Endophilin A1 BAR domain induces membrane tubulation *in vivo*. (A) HUVECs were transfected with plasmids expressing C-teminally EGFP-tagged EndA1-BAR296 (amino acid 1–296 of endophilin-A1), ΔApp, a4, and ΔNT. Cells were GFP-imaged on an epifluorescnce microscope (Olympus IX-71). Fibrous structures were observed exclusively in EndA1-BAR296-expressing cells. Scale, 10 μm. (B) Protein expression of the EndA1-BAR296 and the mutants tagged with EGFP in transfected 293T cells were examined by immunoblotted with anti-GFP antibody. (C) Cells indicated were similarly transfected to (A). Arrowheads indicate the fibrous structures. Scale, 20 μm. (D) Live HUVECs expressing EGFP-tagged EndA1-BAR296 were biotinylated with sulfo-NHS-biotin for 10 min and chased for further 10 min. Covalently bound biotin was visualized using Alexa633-streptavidine. Fluorescnece images for EGFP (left), Alexa633 (center), and merge (right) are shown. Scale, 10 μm. (E) A time lapse images of HUVECs expressing EGFP-tagged EndA1-BAR296 were obtained at the time point (seconds) after the observation (Supplementary Movie 1). EGFP-marked structure grows from the cell periphery towards the center of the cell. Notably, both extension and retraction of GFP-marked structure is observed (numbered arrow heads indicate each extending/retracting structure). Scale, 5 μm.

mutant arm was not changed in a4 mutant irrespective of the bend levels (Supplementary Figure 8). The mutant arm behaves as a rigid body and its structure changes only in the vicinity of the helix kinks when it swings. Therefore, it is unlikely that the flexibility of the mutant dimer can be a result of weakened inter-helix interactions in the arm. Moreover, we could not find any specific structural features in the kink region that might explain the flexible hinge in the swinging-arm mutant as well as the rigid bend in the wild-type BAR dimers of endophilin, amphiphysin, and arfaptin.

In this study, for the first time we could determine the structure of the N-terminal amphipathic helix (helix 0) using a swinging-arm mutant. Our mutant and previous mutation analyses indicated that the N-terminal helical sequence of endophilin-A1 is indispensable for liposome binding (Farsad *et al*, 2001), whereas that of amphiphysin is important but not essential for liposome binding and tubulation (Peter *et al*, 2004). The BAR domain of endophilin-A1 is an acidic polypeptide and the cluster of positive charge at the distal end of the arm is not prominent (Figure 1A). This property can explain the critical role for the helix 0 of the EndA1-BAR in liposome binding by providing additional basic residues. The helix 0 structure suggests that K12, K16 and possibly K8 are in a suitable position for cooperation with the positive charge cluster at the distal end. The amphipathic nature of the helix 0 implies that it can also insert into the membrane and facilitate the membrane curvature formation (Peter *et al*, 2004; Gallop and McMahon, 2005; McMahon and Gallop, 2005). Loss of the membrane-deforming activities of the A66D mutant (Figure 2) and the a4ΔApp mutant (Figure 5D) accounts for the additional mechanism for membrane deformation in addition to the membrane insertion of the helix 0.

The N-BAR of endophilins has one additional step to tubulate membrane. Here, we show that the hydrophobic ridge of the endophilin-specific appendage is inserted into the contacting membrane surface. Our data suggested that the entire ridge of the wild-type BAR domain, about 8 Å in height, is embedded in the layer of lipid head-groups of the contacting membrane leaflet. The embedding of the ridge into the membrane is consistent with the local spontaneous curvature mechanism that is reported very recently (Zimmerberg and Kozlov, 2006). As a protruding structure found in epsin1 induces liposome tubulation by being inserted to one leaflet of the lipid bilayer (Ford *et al*, 2002), the penetration of the hydrophobic ridge can drive the positive curvature by causing asymmetrical expansion of the surface area between two leaflets as shown in Figure 8 (Farsad and De Camilli, 2003).

We further explored the importance of the ridge, rigid crescent shape, and helix 0 in cells. We for the first time showed that N-BAR domain induced membrane invaginations originated from plasma membrane, although other BAR-containing molecules have been reported to induce similar invaginations (Itoh *et al*, 2005). Neither mutant that lacked either the ridge or the helix 0 nor flexible mutant formed the tubular invaginations in cells, indicating the significance of these sub-module structure in cells as suggest by *in vitro* studies. We constructed a series of endorphin-A1-EGFP expression plasmids to delineate the domain for the membrane invagination. Full-length endophilin-expressing cells did not show any tubular formation. Because endophilin consists of BAR domain and an SH domain, SH3-binding molecule such as dynamin may inhibit the extension of membrane invagination. This possibility has been suggested in the membrane invagination found in FBP17 and amphiphysin (Kamioka *et al*, 2004; Itoh *et al*, 2005).

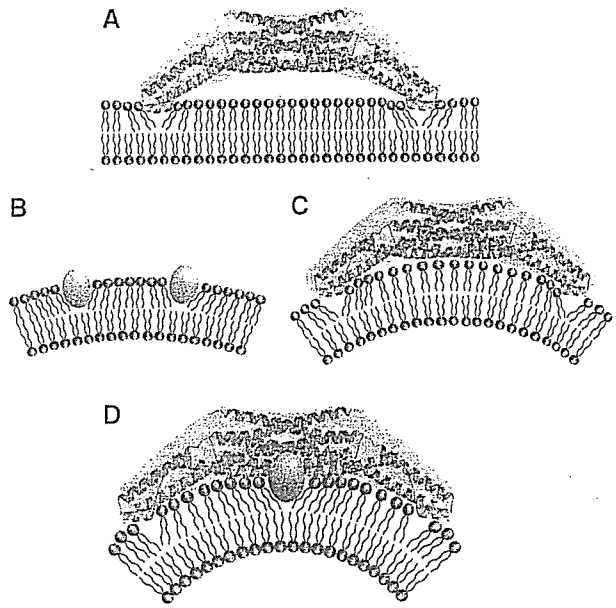

Figure 8 Two potential mechanisms for driving membrane curvature by endophilin-A1. (A) Kissing adhesion of an N-BAR domain on planar lipid bilayer. The helix 0 is essential for the membrane binding. Membrane insertion of the helix 0 is supposed. (B) Insertion of hydrophobic portions of macromolocules into one leaflet can create bilayer surface discrepancy that causes membrane curvature. (C) The simple N-BAR domain, such as amphiphysin and ΔApp, induces membrane curvature by impressing the concave surface onto the membrane. The rigidity of the molecule is required for this mechanism. (D) To drive membrane curvature, the endophilin N-BAR domain uses both the rigid crescent shape-mediated deformation and the insertion of hydrophobic ridge on the concave surface in addition to kissing adhesion of N-BAR to membrane surface.

Collectively, EndA1-BAR uses two newly identified mechanisms to drive positive membrane curvature in addition to the essential binding capacity of helix 0 to the membrane: one by the scaffold mechanism common to the BAR domains and the other by the local spontaneous curvature mechanism caused by the membrane insertion of the ridge (Figure 8D). The ridge, which occupies the bottom of the concave lipid-binding surface, may not work until the main body of the BAR dimer localizes itself to a curved membrane. The ridge then inserts into the bilayer roughly perpendicular to the main body, and thus both deformations will occur in the same direction.

Materials and methods

Protein expression and purification by CRECLE

cDNAs encoding BAR domains (amphiphysin1, 1–239; endophilin-A1, 1–247; endophilin-B1, 1–246 in amino-acid residues) were amplified by PCR from a human brain cDNA library. Recombinant proteins were expressed in *Escherichia coli* as GST-fusions using the pGEX6p3 vector, purified by glutathione-Sepharose, cleaved from the GST-tag using Prescission protease (Amersham Biosciences), and further purified by ion-exchange chromatography (Yamagishi *et al*, 2004). The final polypeptide contained an artificial linker

sequence of GPLGS at the N-terminus. EndA1-BAR proteins except for F202W and a4 mutants were purified by crystallization during Prescission protease cleavage. The method, crystallization by regulated cleavage of large hydrophilic tag (CRECLE), was as follows. Purified GST fusions were concentrated to 20–30 mg/ml in an elution buffer (20 mM glutathione, 100 mM Tris-HCl, pH 8.0, 10 mM DTT, 1 mM EDTA, 1 mM EGTA) and then cleaved by a low concentration of prescission protease (1 U/mg protein or less) at 4°C. Slow increase in the tag-free protein concentration might be suitable for crystallization and more than a half of EndA1-BAR protein could be recovered as 20–100 μm microcrystals. They were washed with a low-salt buffer (20 mM HEPES, pH 7.4, 2 mM DTT, 0.2 mM EDTA, 0.2 mM EDTA) and resolved into a high-salt buffer (350 mM NaCl in the low-salt buffer) and used for further analyses.

Protein crystallization

Seleno-methionine (S-Met) derivatives of the EndA1-BAR domain and its appendage-less mutant (ΔApp) were produced in B834(DE3)pLysS cells using Overnight Express Autoinduction System 2 (Novagen). To make X-ray grade crystals in a cryo-ready condition, modified high salt buffer (50 mM HEPES, pH 7.4, 300 mM NaCl, 100 mM KI, 28% ethylene glycol, 5% glycerol, 25 mM DTT) was used. Crystals of 1 mm size were formed by dialysis against 50 mM CHES, pH 9.5, 260 mM NaCl, 28% ethylene glycol, 5% glycerol, 25 mM DTT, 0.4% benzamidine · HCl at 4°C and were flush frozen at 100 K. Crystals could also be grown by vapor diffusion from a similar protein solution using distilled water as the bath solution. The crystals were equilibrated in 50 mM HEPES, pH 7.4, 150 mM NaCl, 25 mM DTT, 0.4% benzamidine · HCl, 5% PEG 8000 and the saturated amount of xylitol as a cryoprotectant. Some of the crystals were soaked with 0.5 mM oleoyl-L-α-lysophosphatidic acid (Sigma) or malonyl-CoA (Sigma) for 4 days with daily change for the substrates. The a4 mutant crystals were grown by sitting-drop vapour diffusion using a bath solution containing 100 mM HEPES, pH 7.2, 200 mM calcium acetate, 10 mM DTT and 20% (w/v) PEG3350 at 20°C and then flush frozen after brief immersion in the same solution containing 16% DMSO. The wild type and the ΔApp mutant crystals belong to the same space group $I4_1$ and contain one monomer molecule in the asymmetric unit (Supplemental Figure 1). The a4 crystal belongs to $P2_1$ and contains two dimers in the asymmetric unit.

Structural determination

The EndA1-BAR structure was determined using the multiple anomalous dispersion (MAD) method. Multiple-wavelength X-ray diffraction data sets were collected from a single Se-Met crystal (crystal I) at SPring-8 beamline BL44B2 (Supplementary Table I). Single wavelength data sets of another crystal (crystal II) and of a ΔApp crystal used for the refinement were collected at BL45PX. The data set for the a4 mutant was collected at BL38B1. All diffraction data sets were collected at 90 K and were processed using HKL2000 suite (Otwinowski and Minor, 1997). The seven positions out of 10 expected selenium atoms were identified by SOLVE (Terwilliger and Berendzen, 1999). The initial phases calculated by SOLVE with a figure of merit of 0.59 at 3.2 Å resolution were further improved by RESOLVE (Terwilliger, 1999). The density modified MAD map (Supplementary Figure 1) had sufficient quality to trace the polypeptide chain except for the N-terminus and the loop region of the appendage. The model was built with TURBO-FRODO (Roussel and Cambillau, 1996) and refined to the resolutions of 3.1 Å by CNS (Brunger *et al*, 1998). The final model includes 210 residues (residues 26–71 and 84–247), and has an R factor of 23.6% (R_{free} of 26.4%). The ΔApp structure was solved by molecular replacement by MOLREP in the CCP4 suite (CCP4, 1994) and refined to the resolution of 2.9 Å by CNS. The simulated annealing omit electron density map calculated by CNS confirmed the continuous α-helical structure of the replaced region as designed (Supplementary Figure 7). The final model includes 200 amino-acid residues and has an R factor of 23.8% (R_{free} of 26.9%). The a4 mutant structure was solved by molecular replacement using the central core of the EndA1-BAR as a starting model and the arms were manually built (Supplementary Figure 7). The structure was refined to the resolution of 2.4 Å by CNS with an R factor of 21.5% (R_{free} of 26.9%). Main-chain dihedral angles of all non-glycine residues of these three models lie in allowed regions of the Ramachandran plot, with 94.3% for the EndA1-BAR, 94.1% for the ΔApp mutant, and 96.4% for the a4 mutant in most-favored regions, respectively. Graphical representations were prepared using the programs TURBO-FRODO, MOLSCRIPT (Kraulis, 1991), RASTER3D (Merritt and Bacon, 1997), GRASP (Nicholls *et al*, 1991) and Pymol (DeLano, 2002).

Liposome binding and tubulation assays

Liposome sedimentation assay and tubulation assay were as earlier described (Peter *et al*, 2004 see also McMahon lab protocols: http://www2.mrc-lmb.cam.ac.uk/NB/McMahon_H/group/techniqs/techniqs.htm) with slight modifications. Briefly, Folch fraction 1 (Sigma) was used as the lipid source and liposome suspension, 1 mg/ml in liposome buffer (20 mM HEPES, pH 7.4, 150 mM NaCl, 1 mM DTT) was made by sonication. Freshly purified BAR domain proteins were diluted at about 1 mg/ml in the liposome buffer and ultracentrifuged at 400 000 *g* for 10 min just before use. No crystallization occurred at this or lower concentrations. For sedimentation assays, 20 μg proteins were mixed with 25 or 75 μg liposomes in 100 μl of the liposome buffer, incubated for 10 min on ice and ultracentrifuged at 200 000 *g* for 10 min. For tubulation assays, 400 μg/ml proteins were mixed with an equal volume of 400 μg/ml liposomes, left for 10 s to 30 min at room temperature, and then processed for negative staining. Judging from the liposome sedimentation and the tryptophan fluorescence assays, this protein to lipid ratio ensured nearly saturated protein–liposome binding. Magnification was calibrated using a grating replica of 2160/mm.

Tryptophan fluorescence and FRET assay

Fluorescence emission spectra were recorded with a Hitachi F-4500 fluorescence spectrophotometer (Ohki *et al*, 2004). For tryptophan fluorescence assays, 140 μg/ml tryptophan-containing mutants were mixed with 0–200 μg/ml liposomes in the liposome buffer, incubated for 3 min, and excited at 280 nm. For FRET assays, DPH-liposomes were made by adding DPH (Molecular Probe) into lipid solution (1:500 to lipid, w:w). The fluorescence of DPH-liposomes (200 μg/ml) excited at 280 nm was scanned from 400 to 500 nm at 1-min intervals. The first measurement of the 430-nm DPH peak was obtained at about 30 s after mixing with mutant proteins (100 μg/ml).

Cell culture, transfection and surface biotinylation

HUVECs were purchased from Kurabo and cultured in HuMedia-EG2 as described previously (Sakurai *et al*., 2006). 293T cells, CHO cells, Cos7 cells, and NIH-3T3 cells were cultured in DMEM supplemented with 10% fetal bovine serum as described previously (Kamioka *et al*., 2004). Cells were transfected using LipofectAMINE 2000 (Invitrogen). Live HUVECs were biotinylated with 5 mM sulfo-NHS-biotin (Pierce) in Opti-MEM (Invitrogen) for 10 min. They were washed once with Opti-MEM and chased for 10 min with the normal culture medium, and fixed with 2% formaldehyde after a brief wash with Opti-MEM containing 1/20 volume of Avidin D blocking solution (Vector Laboratory) to reduce the cell surface background staining. HUVECs were permeabilized with cold MeOH and biotin was visualized using Alexa633-streptavidine (Molecular Probe).

Supplementary data

Supplementary data are available at *The EMBO Journal* Online.

Acknowledgements

We thank H Nakajima, T Matsu, Y Kawano and H Naitow for technical assistance with SPring-8 beamlines, and H Ago and M Miyano, Structural Biophysics Laboratory, RIKEN Harima Institute at SPring-8, for their helpful advice. This work was supported in part by Grant for Research on Advanced Medical Technology from the Ministry of Health, Labour, and Welfare of Japan, by the Program for Promotion of Fundamental Studies in Health Sciences of the National Institute of Biomedical Innovation (NIBIO), and by Special Coordination Funds for Promoting Science and Technology, Ministry of Education, Culture, Sports, Science and Technology (MEXT) of Japan.

Competing interests statement

The authors declare that they have no competing commercial interests in relation to this work.